Schweizerische Eidgenossenschaft
Confédération suisse
Confederazione Svizzera
Confederaziun svizra

Eidgenössisches Departement für
Umwelt, Verkehr, Energie und Kommunikation UVEK

Bundesamt für Energie BFE

MICRO SOLID OXIDE FUEL CELL ON THE CHIP

Final Report

Written by

Michael Stutz
michael.stutz@ltnt.iet.mavt.ethz.ch

Nico Hotz
nico.hotz@ltnt.iet.mavt.ethz.ch

Dr. Nicole Bieri,

nicole.bieri@ltnt.iet.mavt.ethz.ch

Prof. D. Poulikakos

dimos.poulikakos@sl.ethz.ch

Laboratory of Thermodynamics in Emerging Technologies (LTNT),

Institute of Energy Technology, ETH Zurich

ETH Zentrum, ML J38, Sonneggstr. 3, 8092 Zürich, www.ltnt.ethz.ch

Impressum

Datum: 4. Oktober 2006

Im Auftrag des Bundesamt für Energie, Forschungsprogramm Brennstoffzellen

Mühlestrasse 4, CH-3063 Ittigen

Postadresse: CH-3003 Bern

Tel. +41 31 322 56 11, Fax +41 31 323 25 00

www.bfe.admin.ch

BFE-Projektleiter: Bereichsleiter, bereichsleiter@bfe.admin.ch

Projektnummer: 100459

Bezugsort der Publikation: www.energieforschung.ch

Preface

The aim of this project is the numerical and experimental investigation of hydrocarbon-to-syngas reforming in microreformers for incorporation into an entire micro fuel cell system. Numerical simulations are used to achieve deeper understanding of several determining aspects in such a microreformer. These insights are used to optimize the reforming performance by proper choice of operational and geometrical parameters of a reformer. These numerical results are continued by comprehensive experimental studies.

In the first chapter, the effect of wall conduction of a tubular methane microreformer is investigated numerically. Methane is used as the representative hydrocarbon because its detailed surface reaction mechanism is known. It is found that the axial wall conduction can strongly influence the performance of the microreactor and should not be neglected without a careful a priori investigation of its impact.

In the second chapter, the effect of the catalyst amount and reactor geometry on the reforming process was investigated. It was found that the hydrogen selectivity changes significantly with varying catalyst loading. Thus, the reaction path leading to higher hydrogen production becomes more important by increasing the catalyst surface site density on the active surface. Another unexpected result is the presence of optimum channel geometry and optimum catalyst amount.

In the third chapter of this project, the capability of flame-made $Rh/Ce_{0.5}Zr_{0.5}O_2$ nanoparticles catalyzing the reforming of butane to H_2- and CO-rich syngas was investigated experimentally in a packed bed reactor. The main goal of this study was the efficient reforming of butane at temperatures between 500 and 600℃ for a micro intermediate-temp erature SOFC system. Our results showed that $Rh/Ce_{0.5}Zr_{0.5}O_2$ nanoparticles proved to be a very promising material for butane-to-syngas reforming with complete butane conversion and a hydrogen yield of 77% at 600℃, which is higher than any value reported by other studies.

Content

Introduction

A promising application of fuel cells are miniaturized fuel cell systems generating electric power of the order of a few watts to power small portable electronic devices such as laptops, cameras and cell phones. Small fuel cell systems using hydrocarbons as a fuel combine the high energetic efficiency of fuel cells with the high availability and easy storage of hydrocarbon fuels [1]. Modern materials for Solid Oxide Fuel Cells (SOFCs) lead to higher efficiencies compared to other types of fuel cells at intermediate operating temperatures, namely in the range of 500℃ and 600℃ [2-4]. An important benefit of SOFCs is the possibility of using hydrogen (H_2) and carbon monoxide (CO) simultaneously for electricity production, whereas low temperature fuel cells can not convert CO or even suffer from CO poisoning. This aspect is particularly interesting when the supply of the fuel cells is the reformate from a hydrocarbon reformer which always contains significant amounts of CO. An interesting hydrocarbon fuel for this application is butane (C_4H_{10}), allowing high efficiency for the reforming to a H_2- and CO-rich syngas at moderate temperature similar to the mentioned intermediate temperature of modern SOFCs. Butane can be stored relatively easily in liquid phase at room temperature and low pressure and is widely available.

In the numerical study, methane is used as the representative hydrocarbon because its detailed surface reaction mechanism is known. For higher hydrocarbons, such as butane, it is not known. Thus, the effect of the catalyst amount and reactor geometry on the reforming process of methane in a wall-coated tubular microreactor was investigated.

In the experimental part of this project, the reforming of butane to H_2- and CO-rich syngas was investigated. The reformer was a packed bed reactor containing flame-made $Rh/Ce_{0.5}Zr_{0.5}O_2$ nanoparticles as active catalytic material. The main goal of this study was to investigate the capability of reforming butane at temperatures between 500 and 600℃ for a micro intermediate-temperature SOFC system.

An important impact of the results achieved by this project is the answer to the question how reforming performance in a hydrocarbon microreformer is limited. Generally, reforming reactions can be limited by mass transfer and chemical reaction kinetics. As both numerical and experimental results show, the reforming in such a microreformer is clearly limited by reaction rates rather than by diffusive mass transfer. In other terms, the transport of reacting species and resulting products by diffusion is much faster than the chemical reactions themselves. This leads to the conclusion that tree-like structures as those suggested for PEM fuel cells by Senn and Poulikakos (BFE Project Nr. 87100, Final Report) are not necessary for microreformers operated in the indicated temperature range.

1. Numerical investigation of syngas reforming: Effects of microreactor wall heat conduction on the reforming process of methane

In this section, the effect of wall conduction of an autothermal tubular methane microreformer is investigated numerically. It is found that the axial wall conduction can strongly influence the performance of the microreactor and should not be neglected without a careful a priori investigation of its impact. By increasing the wall thermal conductivity, the maximum wall surface temperature is decreased. Due to the complex exothermic-endothermic nature of the chemistry of reforming, the axial variation of the wall temperature is not monotonic. Methane conversion and hydrogen yield are strongly dependent on the wall inner surface temperature, hence the heat conduction through the channel wall. The equivalence ratio and the wall thickness also significantly affect the reforming effectiveness and must be carefully considered in reactor optimization. Furthermore, it is found that exothermic oxidation reaction mechanisms, especially partial oxidation, are responsible for syngas (hydrogen and carbon monoxide) production near the inlet. Farther downstream, in the oxygen deficient region, endothermic steam reforming is the main hydrogen producing mechanism. By increasing the thermal conductivity, steam reforming becomes stronger and partial oxidation becomes weaker. For all investigated inlet conditions, the highest hydrogen yield is obtained for low thermal conductivity walls.

Numerical simulations are a powerful tool to investigate the fundamental transport phenomena inside a catalytic reactor. There are several approaches for modeling channel reactors. Simple 1-D models neglect gradients along the transverse direction. By using the boundary layer approach, streamwise diffusivity is neglected and parabolic differential equations are obtained [5]. The catalytic reaction at the fluid solid interface has been modeled with detailed reaction schemes [6]. More accurate solutions are obtained with 2-D models, which provide information in the transverse direction along the channel. Simplified 2-D models are employed in order to save computational power. One such simplified model is the 2-D boundary layer model. Its range of validity, is determined after comparisons with complete Navier-Stokes models [7]. Another simplifying modeling approach is the perfectly stirred reactor, which assumes that conversion of reactants to products is determined by the chemical reaction rates rather than the transport processes. Chaniotis and Poulikakos [8] compared this simplified model with a detailed Navier-Stokes model and defined the parametric domain of its validity. All models discussed so far have neglected heat conduction through the reactor channel wall.

Methane is used as hydrocarbon fuel because it is known that the hydrocarbons react in a similar way in comparable conditions [9] and because it is the only hydrocarbon with a known heterogeneous reaction scheme on rhodium.

In order to maximize the efficiency of a fuel cell system, every individual component must be optimized. Large efforts have been dedicated to enhance the power output of a fuel cell, including the improvement of its geometric design [10]. It is also essential to optimize the operating parameters and geometry of the reforming unit, since reforming of hydrocarbons must be performed “on board” to produce hydrogen, especially for portable devices.

In this section, the channel wall heat transfer is included in the 2-D numerical model of an autothermal tubular methane reformer. The major impact of the wall thermal conductivity on the performance of the microreactor is documented and discussed in detail.

1.1 MATHEMATICAL FORMULATION

Transport phenomena in a microchannel reformer can be described by the conservation equations of mass, momentum, energy and species leading to a set of non-linear partial differential equations [11]. The flow inside the microchannel is considered laminar, due to a low inlet Reynolds number. A single channel with all adiabatic walls is modeled in steady state conditions. The fluid is assumed to be an ideal gas mixture that follows Dalton's model.

Heterogeneous reactions take place at atmospheric pressure and usual operating temperatures of a methane reformer [6]. Homogeneous reactions only become important for high pressure applications. Species flux is composed of a concentration driven and a thermal diffusion term, but it does not take into account the pressure diffusion due to low pressure gradients in straight channels. The Peclet number in this study is higher than 10. Therefore the more detailed Maxwell-Stefan formulation, which is used for diffusion dominated flows, is not applied. Furthermore, its computational cost is considerably higher. All surface reactions are specified using a detailed multi-step finite-rate reaction mechanism of oxidation of methane on rhodium [11] with 7 gas phase species, 12 surface adsorbed

site species, and 38 elementary surface reactions [12]. The reaction mechanism has been validated and has shown good agreement with experiments [13].

Monoliths are often employed as catalytic reactors due to their high surface to volume ratio and relatively low pressure drop [14]. The computational domain employed in this study consists of a single cylindrical channel of a monolith reactor (Fig. 1).

Fig. 1: *Sketch of a monolith reactor.*

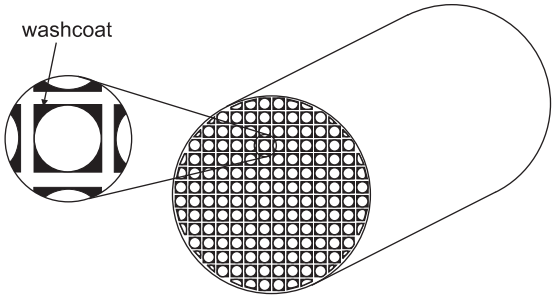

All channels of the monolith are covered by a catalytic washcoat, which fills up the edges of the channels. Hence, the approximation of a cylindrical channel is realistic. The outer boundary of the monolith reactor is assumed to be ideally insulated. Inlet and outlet conditions are uniform; therefore the condition in each channel is the same. Hence, the monolith reactor is approximated as radially symmetric, which is reasonable if the number of channels is large [8, 15]. The flow is always laminar with a Reynolds number of approximately 10 for the inlet flow. The channel reactor is described by the 2-D radially symmetric conservation equations.

The flow enters the reactor with a uniform inlet velocity u = 1 m s^{-1} and a temperature T = 850 K. The channel diameter is d = 1 mm, which is a typical tube diameter of a monolith reactor. The pressure at the outlet is constant p = 1 bar. Inlet composition of the gaseous mixture is defined by the stoichiometric equivalence ratio that is based on the POX reaction mechanism and is written as

$$\phi \equiv \frac{\left(x_{\mathrm{CH4}} / x_{\mathrm{O2}}\right)_{\mathrm{in}}}{\left(x_{\mathrm{CH4}} / x_{\mathrm{O2}}\right)_{\mathrm{stoich}}} = \frac{1}{2}\left(x_{\mathrm{CH4}} / x_{\mathrm{O2}}\right)_{\mathrm{in}} . \qquad (1)$$

Two different models are investigated in this study. The first is the insulated channel model (ICM) and contains only one computational domain, namely the flow inside the channel (Fig. 2a). The second model is the conductive wall model (CWM), which consists of two computational domains. The first domain is the flow channel and the second one is the thermally conductive channel wall (Fig. 2b).

Fig. 2: *(a) Computational domain and boundary conditions of the insulated channel model (ICM) and (b) of the conductive wall model (CWM).*

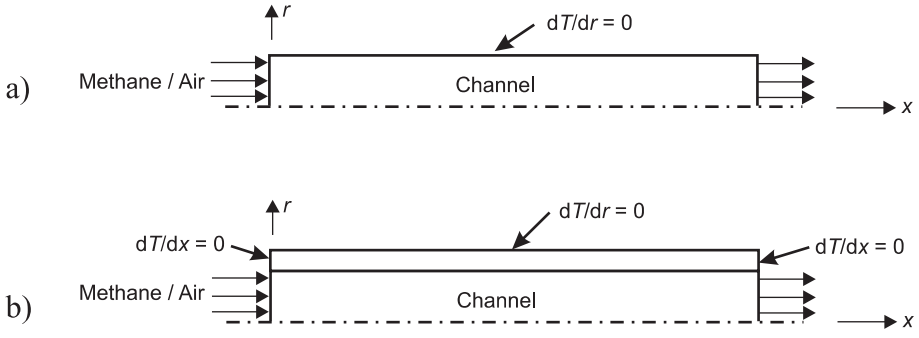

Previous 2-D investigations have already been performed using the ICM model [8]. The channel wall inner surface where the catalytic reaction takes place is adiabatic. In the CWM model the catalytic

reaction takes place at the interface between wall and channel. The boundary condition of the numerical model at the outer diameter of the wall is set to be adiabatic, because the monolith reactor is approximated as radially symmetric. Also adiabatic are the wall boundaries at the inlet and outlet. The channel wall represents the solid part of the monolith. The thickness of the solid part of a real monolith reactor with washcoat is not exactly uniform. Therefore, the wall thickness used in the numerical model represents an averaged half-thickness of the solid part. A typical monolith material is cordierite, which is a ceramic with a thermal conductivity k = 2.76 W m^{-1} K^{-1}.

Important characteristics for methane reforming are methane conversion and hydrogen yield. Methane conversion is defined as the ratio between converted methane at a position along the channel and the inlet flux of methane. It reads

$$\eta \equiv \frac{\dot{m}_{\mathrm{CH4,in}} - \dot{m}_{\mathrm{CH4}}}{\dot{m}_{\mathrm{CH4,in}}} . \qquad (2)$$

Hydrogen yield characterizes the performance of the reactor with respect to the hydrogen production. It is the ratio of the produced hydrogen to the theoretical maximum amount of hydrogen

$$\psi \equiv \frac{1}{2} \frac{\dot{m}_{\mathrm{H2}} / M_{\mathrm{H2}}}{\dot{m}_{\mathrm{CH4,in}} / M_{\mathrm{CH4}}} . \qquad (3)$$

1.2 RESULTS AND DISCUSSION

Chaniotis and Poulikakos [8] identified the equivalence ratio 0.6 < ϕ < 1.0 as the region of interest of an insulated wall channel reactor due to high hydrogen yield and low catalyst deactivation. The parameters that vary in the present study are the thermal conductivity, the equivalence ratio, and the wall thickness. The thermal conductivity varies in the range from k = 0.0276 W m^{-1} K^{-1} which represents good thermal insulators such as expanded polystyrene to k = 0.276 W m^{-1} K^{-1} that is typical for polymers to k = 2.76 W m^{-1} K^{-1} that represents ceramics (e.g. cordierite) to k = 27.6 W m^{-1} K^{-1} (e.g. aluminum oxide) to k = 276 W m^{-1} K^{-1} representing metals (e.g. aluminum: k = 237 W m^{-1} K^{-1}). The equivalence ratio variation ranges from the fuel lean regime to the stoichiometric condition (0.7 ≤ ϕ ≤ 1.0). The wall thickness of the numerical model is varied between t = 0.0375 mm and t = 0.15 mm.

1.2.1 Equivalence ratio ϕ = 0.8

The temperature of the gaseous mixture at the channel catalytic inner surface is plotted for the ICM and the CWM with different thermal conductivities in Fig. 3a.

For all models and thermal conductivities, the temperature varies non-monotonically along the axial direction featuring a maximum in the first fifth of the channel length. Therefore the surface reactions are exothermic in this segment of the channel and endothermic in the second much longer segment. The CWM with the lowest thermal conductivity (k = 0.0276 W m^{-1} K^{-1}) has nearly the same temperature distribution as the ICM. This is physically correct, because the ICM is the solution if the wall thermal conductivity approached zero. The CWM with the highest thermal conductivity (k = 276 W m^{-1} K^{-1}) has almost uniform wall temperature. This also logical since the isothermal wall solution is equivalent to the solution of the thermal conductivity approaching infinity. The numerical computation shows that the lower the thermal conductivity the higher the maximum wall temperature. An interesting outcome is the wall temperature at the outlet that shows non-monotonic behavior with respect to the thermal conductivity.

The gas mixture temperature averaged over the channel cross section for different thermal conductivities is shown in Fig. 3b. All curves start from the inlet temperature T = 850 K and reach a maximum temperature, featuring a non-monotonic behavior. The maximum average gas mixture temperature (Fig. 3b) is lower than the maximum wall temperature of the corresponding curve (Fig. 3a). The reason for it is the presence of the overall exothermic surface reactions on the channel wall that heats up the gaseous mixture. Thus, the channel wall temperature is higher than the corresponding mean gas temperature at the same axial position. The location of maximum temperature is farther downstream than the location of maximum temperature of the channel wall, due to mass transport and heat transfer effects. Again it is found that the lower the wall thermal conductivity, the higher the maximum average gas mixture temperature.

Fig. 3: *(a) Temperature at the channel wall, (b) mean gas mixture temperature, (c) methane conversion, and (d) hydrogen yield along the channel for an equivalence ratio ϕ = 0.8. (-) represents the ICM model, (- -) represent the CWM models with increasing wall heat conductivity along the direction of the arrow.*

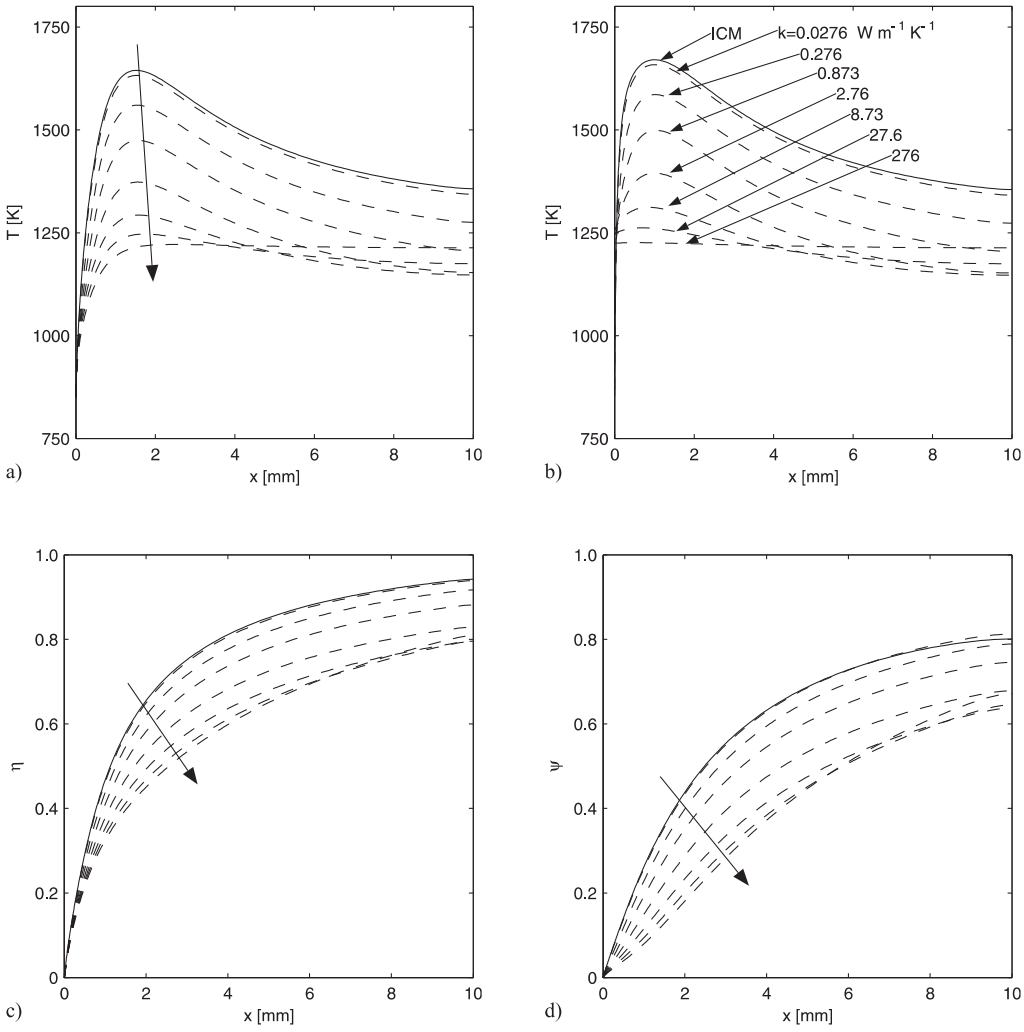

For all investigated models, the methane conversion rises monotonically along the channel (Fig. 3c). The conversion is faster at the beginning of the channel and slower downstream. For the first half of the channel it is evident that the lower the thermal conductivity the higher the methane conversion. In the second half of the channel, there is no monotonic behavior with respect to thermal conductivity anymore. The total conversion of the highest conductivity wall (k = 276 W m^{-1} K^{-1}) exceeds that of k = 27.6 W m^{-1} K^{-1} and k = 2.76 W m^{-1} K^{-1}.

The hydrogen yield rises monotonically along the channel for all investigated cases (Fig. 3d). In the first half of the channel it can be seen that the lower the thermal conductivity the higher the hydrogen yield. This behavior does not hold for the second half of the channel. The highest hydrogen yield is reached by the CWM with the lowest thermal conductivity k and the lowest yield corresponds to k = 2.76 W m^{-1} K^{-1}. The non-monotonic behavior with respect to the thermal conductivity k in the second part of the channel is of interest and is discussed below.

The oxygen concentration at the channel wall nearly reaches zero for all models and for x > 3 mm (Fig. 4a). Therefore POX and TOX reactions that use oxygen as a reactant hardly take place for x > 3 mm. Furthermore two important exothermic carbon gasification (CG) processes cannot occur without oxygen consumption. They are C + O_2 → CO_2 (ΔH = -393.5 kJ/mol at STP) and C + 0.5 O_2 → CO (ΔH = -110.5 kJ/mol at STP). Thus, for x > 3 mm carbon can only desorb by reacting with water: C + H_2O → CO + H_2 (ΔH = +131.3 kJ/mol at STP), which is an endothermic reaction.

Fig. 4: *(a) Oxygen, (b) water, (c) carbon dioxide, and (d) carbon monoxide molar fraction at the channel wall along the channel for an equivalence ratio ϕ = 0.8. (-) represents the ICM model, (- -) represent the CWM models with increasing wall heat conductivity along the direction of the arrow.*

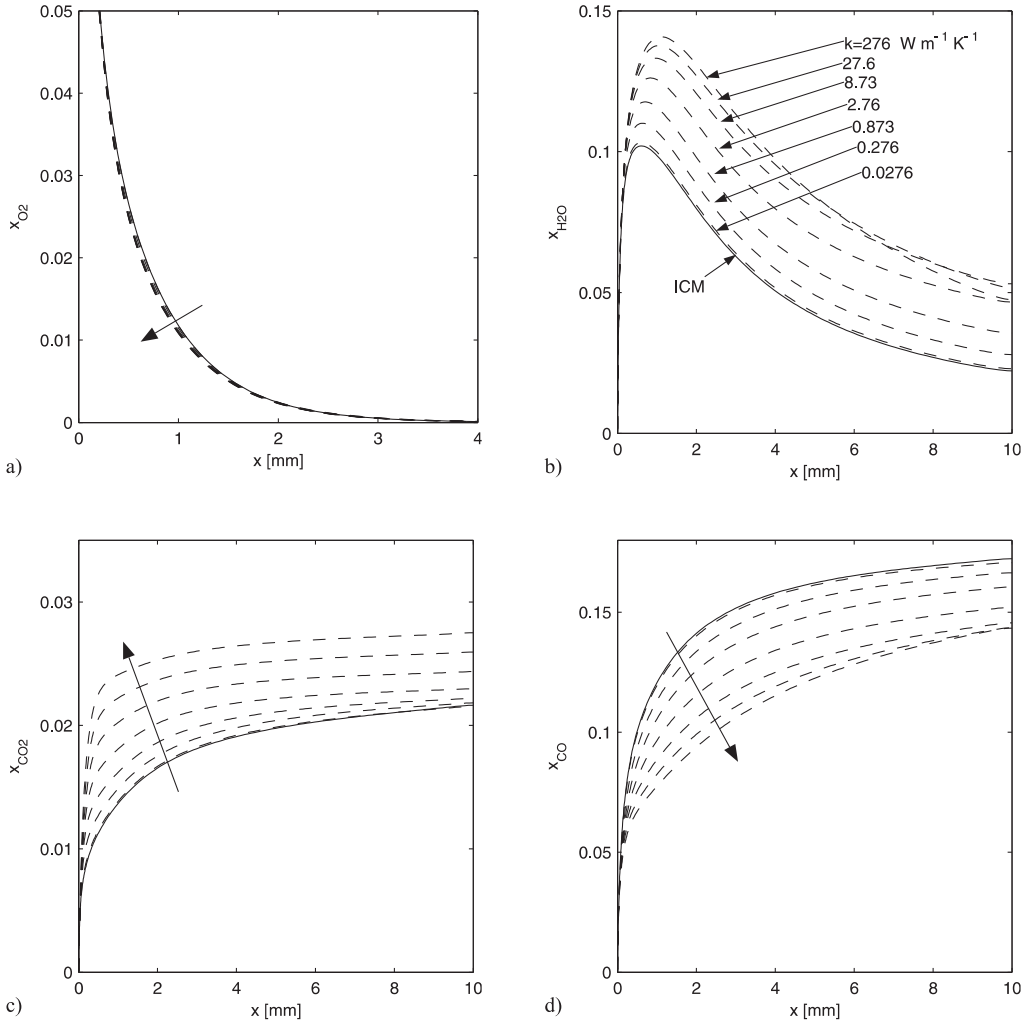

The water concentration increases monotonically to reach a maximum concentration located between x = 0.6 mm (for ICM) and x = 1.1 mm (for CWM, k = 276 W m^{-1} K^{-1}) (Fig. 4b). Thus, in front of the maximum water concentration point, the dominant reaction is the water producing TOX, and behind this point, the dominant reactions are SR and WGS that both consume water. It can be seen that the higher the wall conductivity the higher the maximum water concentration and therefore the stronger the TOX. Heat transport through the channel has an important influence because the maximum wall temperature decreases with increasing the thermal conductivity.

The carbon dioxide molar fraction increases monotonically along the channel for all models (Fig. 4c). The molar concentration of carbon dioxide near the inlet is around 10 times lower than the molar water concentration. The only water and carbon dioxide producing mechanism that is important at the beginning of the channel (WGS is barely active) is TOX. Therefore, the carbon dioxide concentration should be around half the water concentration. In order to solve this contradiction the mechanistic reaction scheme must be modified. A splitting of TOX in two parts is proposed. The first part is the carbon monoxide generating process (COG) $CH_4 + 1.5\ O_2 \rightarrow CO + 2\ H_2O$ (ΔH = -519.3 kJ/mol at STP) and the second part is the oxidation of carbon monoxide (OXCO) $CO + 0.5\ O_2 \rightarrow CO_2$ (ΔH = -172.5 kJ/mol at STP). If these two parts are combined, the TOX mechanism is obtained. The splitting of TOX in two parts is already proposed for homogeneous reactions [16]. Thus, near the inlet COG is more active than OXCO for all thermal conductivities. The higher the thermal conductivity the stronger the COG and the weaker the OXCO.

It is visible in Fig. 4d that the lower the thermal conductivity of the wall the higher the carbon monoxide mole fraction in the first half of the channel, hence the stronger the POX. The curves are monotonically increasing along the channel for all models, therefore at least one of the CO producing

reactions POX, SR, COG, and dry reforming (DR), expressed by $CH_4 + CO_2 \rightarrow 2\ CO + 2\ H_2$ (ΔH = +247.3 kJ/mol at STP) must be active everywhere inside the channel. For x > 3 mm, where hardly any oxidation reaction take place, the carbon monoxide producing SR is stronger than the carbon monoxide consuming WGS because the CO concentration constantly increases along the channel.

The carbon dioxide consuming DR is weak because the carbon dioxide concentration constantly increases along the channel (Fig. 4d). It is worth noting that for x > 3 mm, the higher the thermal conductivity the stronger the SR due to steeper curves which indicate higher production rates.

1.2.2 Variation of equivalence ratio

The equivalence ratio determines the ratio between carbon and oxygen atoms at the inlet and therefore influences the activity of the reactions. It is found that the mean gas mixture temperature at the outlet of the channel is dependent both on the equivalence ratio and on the thermal conductivity of the channel wall (Fig. 5a).

Fig. 5: *(a) Mean gas mixture temperature, (b) methane conversion, (c) hydrogen yield, and (d) surface site fraction of adsorbed carbon at the outlet for different equivalence ratios ϕ.*

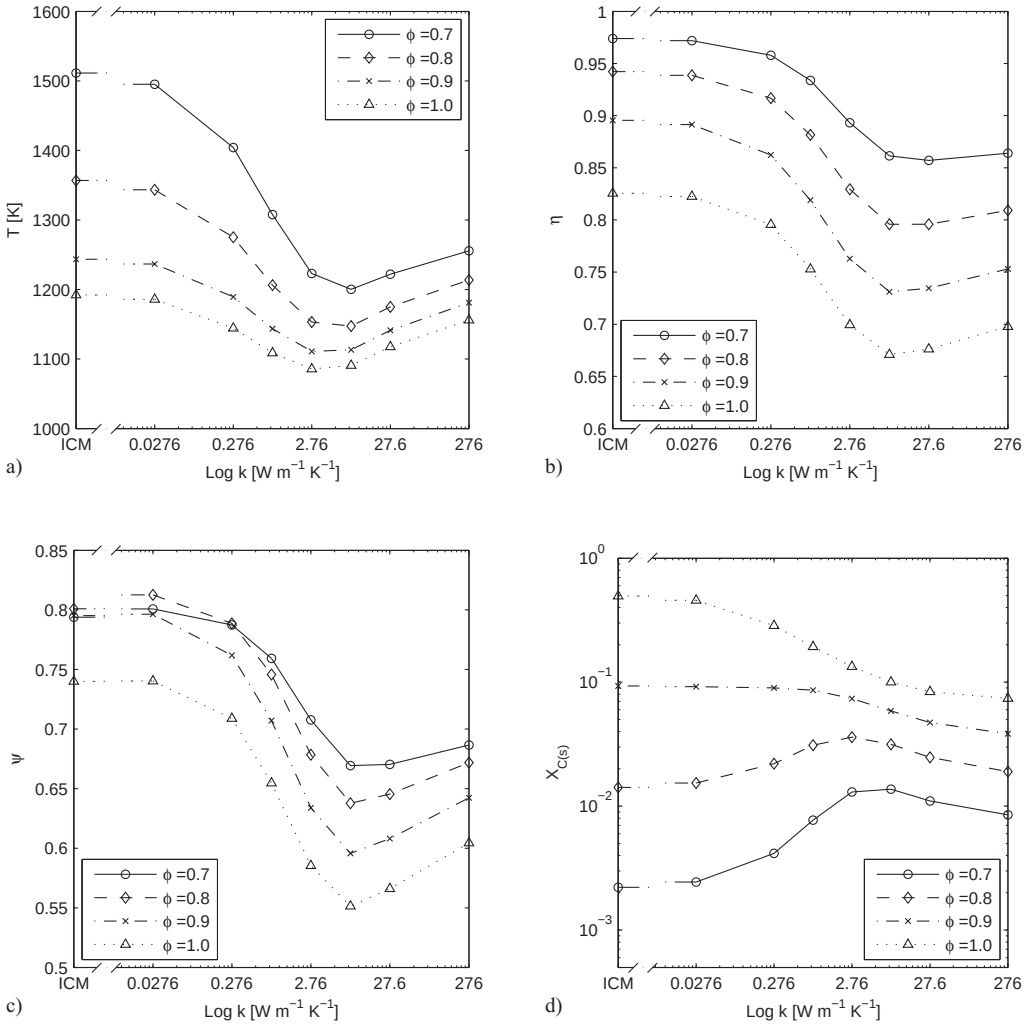

The lower the equivalence ratio ϕ, the higher the outlet temperature for the same thermal conductivity, because the lowest equivalence ratio employed ϕ = 0.7 is nearest to the stoichiometric equivalence ratio of the highly exothermal TOX (ϕ_{stoich} = 0.25) and COG (ϕ_{stoich} = 0.33) reactions. For all equivalence ratios employed, there is a minimum outlet temperature obtained for thermal conductivities in the range $k \approx 1 - 10$ W m^{-1} K^{-1}. The outlet temperature is mainly influenced by the heat producing COG, OXCO, and POX, the heat consuming SR and the heat transport through the channel wall. For a low thermal conductivity the heat transport is weak, hence SR barely cools down the flow, which leads to a high outlet temperature. In the minimum outlet temperature range, the

cooling effect of the SR is strong and prevails over the heat conduction mechanism that distributes the heat in the axial direction. For higher thermal conductivities, the heat transport becomes more important than the cooling effect of SR. Thus, higher outlet temperatures are obtained.

At the channel outlet it is visible that the lower the equivalence ratio the higher the methane conversion for a given thermal conductivity (Fig. 5b). For a constant equivalence ratio, the maximum conversion is obtained with minimal thermal conductivity of the channel wall, due to strong oxidative reactions near the channel inlet. Minimum conversion is reached for thermal conductivity of about $k \approx 10 - 300$ W m^{-1} K^{-1}. For even higher thermal conductivities the methane consumption by SR in the second half of the channel compensates the weaker oxidative reactions near the inlet, therefore higher total methane conversion is obtained. The amount of methane conversion can differ up to 16% for the two employed models ICM and CWM.

Hydrogen yield is also both dependent on the wall thermal conductivity and the equivalence ratio (Fig. 5c). The highest hydrogen yield is obtained for the CWM with the lowest thermal conductivity for each equivalence ratio. The hydrogen yield for the ICM is slightly lower. This is due to the detailed modeling of the channel and the surface reaction mechanism. Noticeably a small wall thermal conductivity increases the activity of SR more than it reduces the POX mechanism. Hence, the performance of the reactor is enhanced. By further increasing the wall conductivity, the reduction of activity of the POX mechanism prevails over the increase of activity of the SR. Thus, the hydrogen yield decreases to finally reach a minimum for a thermal conductivity of around $k = 8$ W m^{-1} K^{-1} where the COG and POX mechanisms are weak and the SR cannot sufficiently compensate the hydrogen production. By further increasing the thermal conductivity, the SR mechanism becomes stronger and balances better the weaker oxidative reactions. The globally highest hydrogen yield of 0.81 is obtained with equivalence ratio $\phi = 0.8$ and thermal conductivity $k = 0.0276$ W m^{-1} K^{-1}. For technical applications with ceramic monoliths ($k \approx 2.76$ W m^{-1} K^{-1}) the highest calculated value is obtained for an equivalence ratio $\phi = 0.7$. The trend implies that hydrogen yield is increased further for even lower equivalence ratios. In all, hydrogen yield can vary significantly up to 20% for different wall conductivities.

The higher the equivalence ratio, the lower the carbon concentration at the channel wall for the same thermal conductivity, because more oxygen atoms are present to react with carbon atoms (Fig. 5d). For the equivalence ratio $\phi = 1.0$ the maximum carbon deposition is obtained from the model with the least conductive walls, or the ICM respectively. This is due to the weakly water consuming CG that is more active if heat is conducted through the walls. For the equivalence ratio $\phi = 0.9$ the curve has a similar shape with the maximum on the low conductivity side and the minimum on the high conductivity side. The curves for the equivalence ratio $\phi = 0.8$ and $\phi = 0.7$ are different. Carbon deposition plays a major role in autothermal reforming because of catalyst deactivation. Low carbon site fraction is therefore desired.

Fig. 6: *a) Maximum wall temperature and b) location of the maximum wall temperature along the channel for different equivalence ratios ϕ.*

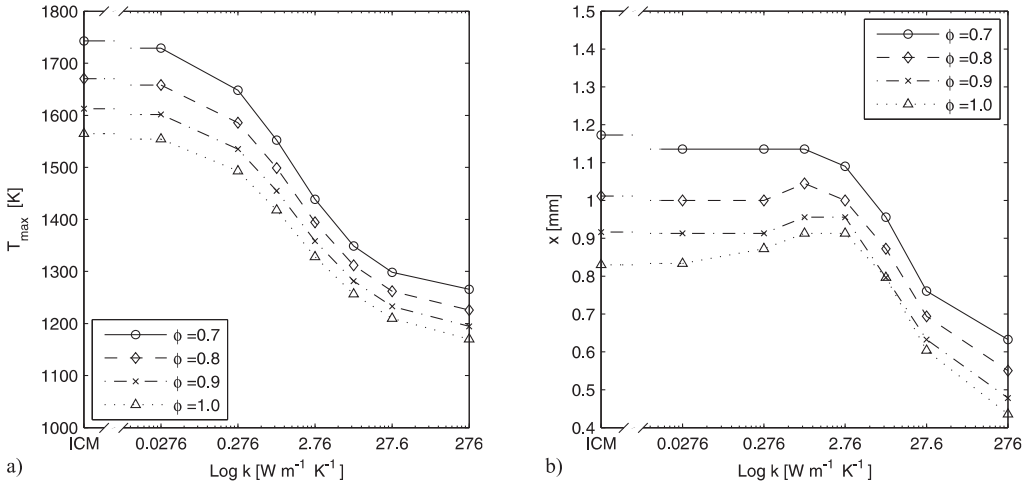

The maximum wall temperature is an important parameter in the reforming processes, because a high temperature can decompose the channel wall material, catalyst, catalyst support and/or washcoat. Thus, low maximum wall temperatures are desired. Fig. 6a shows evidence that the lower the equivalence ratio, the higher the maximum temperature for the same wall conductivity because a lower equivalence ratio provides more oxygen to the reactive sites to feed the exothermic oxidative reactions.

For a constant equivalence ratio, the highest value of the maximum wall temperature is obtained for the ICM, because the heat produced at the catalytic wall cannot be distributed through the channel wall. If the wall thermal conductivity is increased, the value of maximum wall temperature decreases. The endothermic SR, which is more active for conductive wall models, further lowers the value of maximum temperature. The value of maximum temperature can differ up to 477 K for the different cased considered.

The location of maximum wall temperature is an indicator for the transition point (TP) from overall exothermic to overall endothermic reactions. It can be seen that the lower the equivalence ratio the farther downstream the TP for a given thermal conductivity (Fig. 6b) because a lower equivalence ratio provides more oxygen at the inlet and therefore can feed the exothermic reactions longer. The competitive mechanisms that determine the location of the TP are heat conduction through the walls that tends to shift the maximum wall temperature toward the middle of the channel, and SR that tends to shift the TP toward the inlet and is more active for conductive walls. For a constant equivalence ratio, the TP is farthest upstream for the most conductive walls due to the dominant SR.

1.3 CONCLUSIONS

The effect of heat conduction through the channel wall of an autothermal methane microchannel reformer has been investigated. Two different models have been employed, one limited model consisting only of the inner channel domain with an adiabatic boundary neglecting wall conductivity, and the other (the main focus of the work) consisting of two domains, the flow channel and the thermally conductive channel wall. The outer wall boundary is assumed adiabatic due to symmetry conditions in a monolith.

The thermal modeling of the channel wall proved to be important in predicting the reactor behavior. To this end, the value of the maximum channel wall temperature can differ up to 477 K. Maximum methane conversion is obtained if the channel wall is not conductive. A conductive channel wall yielded methane conversion up to 16% lower, which is a marked reduction of reactor performance. The hydrogen yield was highest for a low wall thermal conductivity k = 0.0276 W m^{-1} K^{-1} and an equivalence ratio ϕ = 0.8. By increasing the thermal conductivity the hydrogen yield was reduced up to 20%. It is deemed necessary to model the channel wall in order to predict the reactor performance correctly.

In technical applications, where the channel walls are made either of ceramics or metals, investigation of the channel wall conduction has a substantial effect on accuracy; neglecting the thermal conductivity of the channel wall overpredicts significantly the methane conversion, hydrogen yield, and maximum wall temperature.

2. Numerical investigation of syngas reforming: Optimization of methane reforming in a microreactor - effects of catalyst loading and geometry

In this chapter, the effect of the catalyst surface site density (catalyst amount) and reactor geometry on the reforming process of methane in a wall-coated, single-channel microreactor is investigated numerically to use the insights from Chapter 1 to optimize the performance of a microreactor. Such a reactor, consisting of a tubular flow channel and a thermal conductive channel wall, is a good representation of micro-fabricated channels and monoliths. Methane is used as a representative hydrocarbon because its detailed surface reaction mechanism is known. It is found that the hydrogen selectivity changes significantly with varying catalyst loading, which is an unexpected result. Thus, the reaction path leading to higher hydrogen production becomes more important by increasing the catalyst surface site density on the active surface. This is due to the splitting rate of methane and water, which is a function of catalyst density. Furthermore, this study shows the importance of scaling the inlet volume flow not only by the reactor volume (gas space velocity) but also by the catalyst amount (catalyst space velocity). Another unexpected result is the presence of optimum channel geometry and optimum catalyst amount if the gas space velocity and the catalyst space velocity are constant. This enforces the necessity of coordinating the channel diameter, the inlet volume flow rate, and the catalyst amount in order to obtain a maximum reformer performance. Furthermore, it is absolutely necessary to specify the catalyst amount, the inlet conditions and the geometry in order to characterize sufficiently a catalytic reactor.

Several recent investigations [6, 8, 9] show that two parameters are crucial for the characterization of a catalytic reformer: the gas space velocity (*GSV*) and the catalyst space velocity (*CSV*). The *GSV* is defined as the ratio of gas volume flow at the reactor inlet to the total reactor volume and reads

$$GSV = \dot{V}_{\text{in}} / V_{\text{reactor}} . \tag{4}$$

More specifically, the *CSV* is defined as the ratio of gas volumetric flow rate through the reactor inlet to the amount of catalyst on the reactor surface. The amount of catalyst in experiments is often defined in terms of mass [17]. More accurately, it should be quantified by the catalytically active sites n_{cat}. Thus, in this study the *CSV* is defined as

$$CSV = \dot{V}_{\text{in}} / n_{\text{cat}} . \tag{5}$$

If the reforming process is fully transport limited, the reactor performance is constant for constant *GSV*. If the reforming process is fully reaction rate limited, the reactor performance is constant for constant *CSV*. In practice, the reactor performance depends on both *GSV* and *CSV*. However, the coupled and simultaneous influence of both these parameters has not been considered in the literature.

In this section, the effect of catalyst loading and reactor geometry defined by *GSV* and *CSV* on the performance of a methane microreactor is investigated. The channel wall heat transfer is included in the axisymmetric numerical model of an autothermal tubular reformer, described by an explicit model of the flow channel and a detailed elementary surface reaction mechanism consisting of 38 steps.

2.1 RESULTS AND DISCUSSION

Three different cases are investigated in this study, focusing on the effect of the *CSV*, *GSV* and geometry (channel diameter) on the reformer behavior. In the first part, the geometry and *GSV* are kept constant and only the *CSV* is varied. In the second part, the influence of *CSV* on reactor performance is studied. The *GSV* and geometry are left unchanged. The last part deals with the behavior of different channel diameters at constant *CSV* and *GSV*.

2.1.1 Constant GSV, variable CSV

The influence of catalyst amount on the catalytic reaction process is investigated for a constant reactor geometry, constant inlet conditions, and constant *GSV* = 100 s^{-1} (u_{in} = 1 m s^{-1}) for different values of *CSV*. In these cases, a low *CSV* corresponds to a high catalyst amount (Eq. (5)) and therefore a high catalyst density on the interface between flow channel and channel wall. The catalyst amount is

represented by the number of exposed active catalyst sites (in kmol) on the catalytically active rhodium [18].

Methane conversion is plotted for different *CSV* in the range between *CSV* = 0.6x10^6 m^3 kmol^{-1} s^{-1} and *CSV* = 3.7x10^6 m^3 kmol^{-1} s^{-1} (Fig. 7a).

Fig. 7: (a) Methane conversion and (b) hydrogen yield along the channel for different CSV at a constant GSV = 100 s^{-1}.

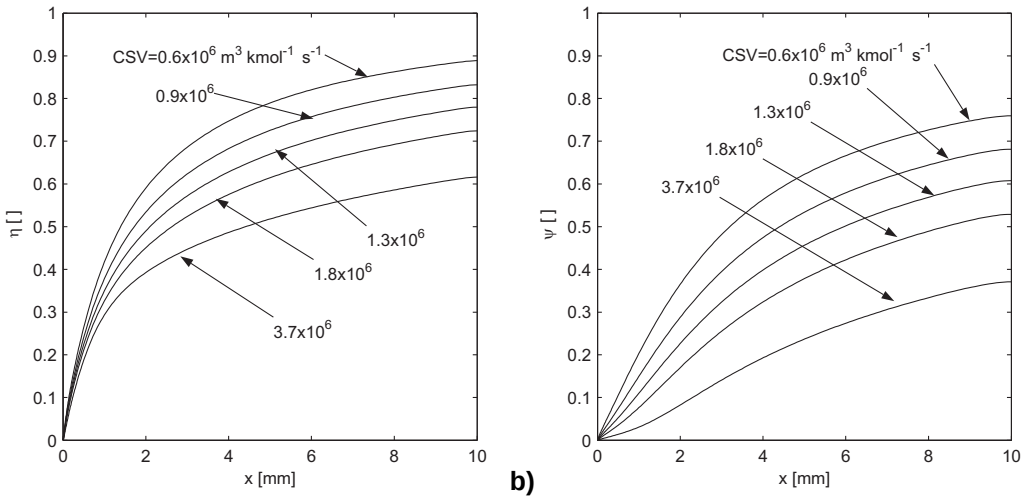

These values correspond to the number of active catalyst sites n_{cat} = 12.8x10^{-13} kmol and n_{cat} = 2.1x10^{-13} kmol, respectively. The methane conversion is monotonic with respect to *CSV* all along the channel: the lower the *CSV*, the higher the methane conversion. This is physically correct, because the higher the amount of catalyst, the higher the rates of adsorption and catalytic reaction. Maximum methane conversion (η = 88.9%) is obtained for a *CSV* = 0.6x10^6 m^3 kmol^{-1} s^{-1}, minimum methane conversion (η = 61.6%) is calculated for a *CSV* = 3.7x10^6 m^3 kmol^{-1} s^{-1}.

The hydrogen yield also shows a monotonic dependence on the *CSV* (Fig. 7b). Thus, the lower the *CSV is*, the higher the hydrogen yield. This result is also no surprise, since a large amount of catalyst implies a high performance of the reactor. The maximum hydrogen yield ψ = 75.9% is obtained for the *CSV* = 0.6x10^6 m^3 kmol^{-1} s^{-1} and the lowest hydrogen yield ψ = 37.1% for *CSV* = 3.7x10^6 m^3 kmol^{-1} s^{-1}. By comparing the difference between maximum and minimum methane conversion (27.3%) with the difference between maximum and minimum hydrogen yield (38.8%), it is clear that methane conversion and hydrogen yield are not equally sensitive to the amount of catalyst. Therefore, the variation of the number of catalytically active sites does not affect all reactions in the same way. This aspect is investigated by studying the temperature and the mole fraction of the individual components at the channel wall.

The temperature at the channel wall increases along the axial direction until a maximum is reached (Fig. 8).

After this point the endothermic reactions (mainly SR) are responsible for the monotonic decrease of wall temperature in the axial direction [11]. It is visible that the higher the *CSV*, the higher the maximum wall temperature. Thus, decreasing the catalyst amount leads to an increase of the rate of exothermic reactions. The temperature drop from the maximum temperature to the outlet temperature of the wall is a good indicator of the intensity of the endothermic reactions. The difference from the maximum to the outlet temperature is monotonic with respect to the *CSV* and ranges from 173 K for the highest *CSV* to 246 K for the lowest *CSV*. Therefore SR, which is the dominant endothermic reaction in that part of the channel, is strong if the amount of catalyst is high. Hence, by increasing the amount of catalyst, the oxidative exothermic reactions near the inlet become weaker and the endothermic SR becomes stronger. The oxygen mole fraction at the channel wall is almost identical for all investigated cases (Fig. 9a).

Fig. 8: *Temperature at the channel wall along the channel for different CSV at a constant GSV = 100 s^{-1}.*

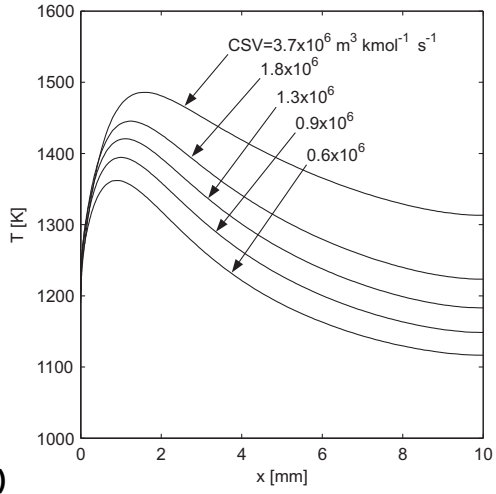

a)

Fig. 9: *(a) Oxygen, (b) water, (c) carbon monoxide, and (d) carbon dioxide mole fraction at the channel wall along the channel for different CSV at a constant GSV = 100 s^{-1}.*

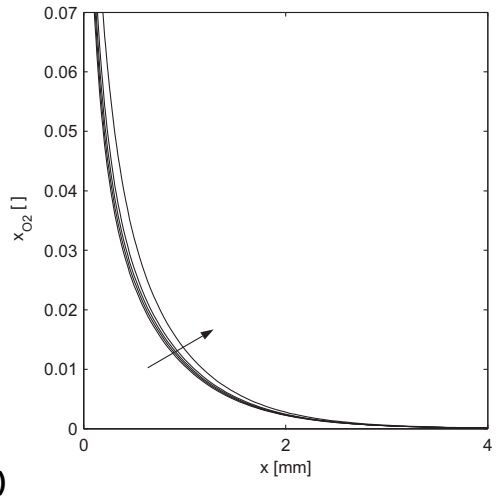

a)

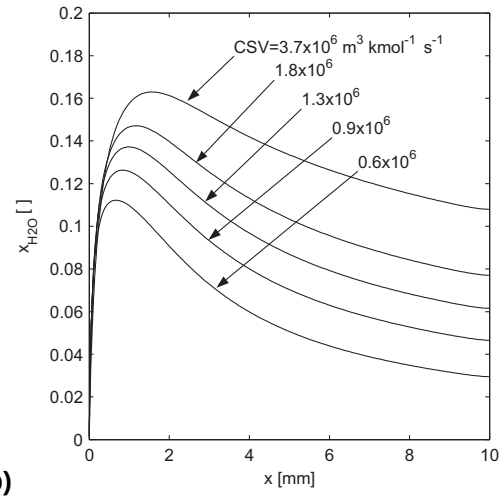

b)

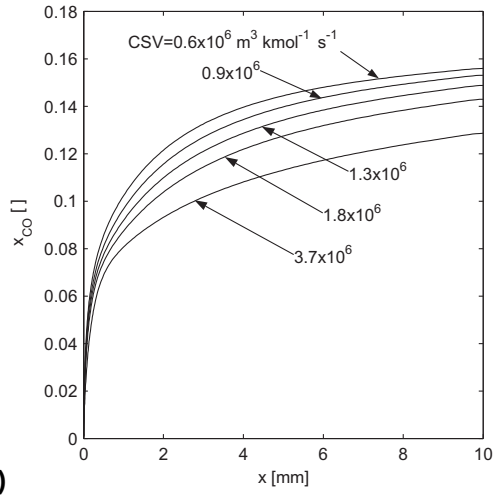

c)

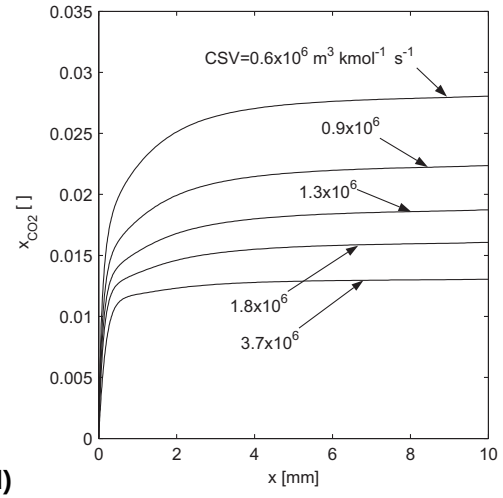

d)

It decreases monotonically along the channel to reach a point where hardly any oxygen is left to support oxidative catalytic reactions. In this study, this is defined as the oxygen deficient region, where oxygen mole fraction is below 0.1%, which corresponds to an oxygen conversion of about 99.4%. For all *CSV*, the oxygen deficient region starts at nearly the same location (x = 2.7 mm). Therefore, the oxygen mole fraction is hardly dependent on catalyst density. Only the curve for the highest *CSV*, corresponding to a minimum catalyst amount, can be clearly distinguished from the other curves.

Thus, it is evident that the adsorption process of oxygen is very fast and the gas-phase transport inside the flow channel determines the adsorption rate of oxygen. Influence of the amount of catalyst becomes only important if a certain level is reached. The water mole fraction at the channel wall increases almost at equal initial rates for all *CSV* right behind the inlet (Fig. 9b). However, the maximum value reached is dependent on the amount of catalyst; the higher the *CSV* the higher the maximum water mole fraction. Therefore the lower the amount of catalytically active sites, the higher the water production rate. Thus, TOX and COG are stronger for the models with high *CSV*. This can be explained by the adsorption process, which is different for methane and oxygen. The sticking coefficient of methane on rhodium γ = 0.008 is of the same order of magnitude as that of oxygen on rhodium γ = 0.01.

However, once oxygen has been adsorbed, it is found on the rhodium surface as two single adsorbed atoms O(s). If methane has been adsorbed, the hydrogen-carbon bonds have not split immediately. An adsorbed methane molecule CH_4(s) first has to split the carbon-hydrogen bonds and eject the hydrogen atoms to become CH_3(s), then CH_2(s), then CH(s) and finally C(s). Eventually the carbon atom is ready to bond an oxygen atom. These splitting reactions always need free rhodium sites if a reaction with oxygen is avoided. If these sites are scarce, the probability of oxygen bonding to hydrogen is higher than the bonding of oxygen to carbon leading to strong COG and TOX.

The location of maximum water mole fraction, which is an indicator for the onset of water consuming reactions, is also different for the investigated models. It can be seen that the higher the *CSV* the later the onset of SR (Fig. 9b), which is the dominant water consuming reaction [11]. Adsorption rate of water on rhodium is very high (γ = 0.1). Hence, the location of maximum water mole fraction is not influenced by the amount of catalyst. Surface reactions have to be rate limiting. If the water molecule adsorbs on the surface, it is present as H_2O(s). The hydrogen-oxygen bonds first have to split before the oxygen atom can connect to a carbon atom. The splitting procedure always needs free rhodium sites. If these sites are scarce, the splitting is slow. Thus, the more catalytically active sites are available, the faster the water splitting on the surface and the more active the SR. This result is confirmed by comparing the difference between the maximum water mole fraction and the outlet mole fraction at the wall, which is an indicator of the activity of SR. The higher the *CSV*, the lower the difference and therefore the lower the activity of SR.

The mole fraction of carbon monoxide increases monotonically along the channel for all *CSV* (Fig. 9c). It is visible that the lower the *CSV* the higher the carbon monoxide mole fraction at the wall at every axial position. This result confirms the adsorption mechanism, described above. Therefore, a large number of catalytically active rhodium sites enhances the generation of carbon monoxide.

The carbon dioxide mole fraction is monotonic with respect to *CSV* at every axial position; the lower the *CSV* the higher the carbon dioxide mole fraction (Fig. 9d). This is again explained by the intrinsic surface reaction mechanism. If the amount of surface sites is low, the adsorbed oxygen atoms O(s) have the tendency to react with adsorbed hydrogen H(s), which is released from methane. Once carbon monoxide has been formed, there is not much oxygen left on the surface to form carbon dioxide. If the catalytically active surface sites are abundant, the probability is higher for an adsorbed carbon monoxide molecule to encounter an adsorbed oxygen atom to form carbon dioxide. In the oxygen deficiency region, the carbon dioxide mole fraction does not increase significantly anymore, indicating low activity of WGS.

The shape of the methane conversion curves (Fig. 7a) and the hydrogen yield curves (Fig. 7b) for different *CSV* can now be explained. In the oxygen rich region close to the inlet and for high *CSV* splitting of the carbon-hydrogen bond is slow. Thus, the surface adsorbed oxygen atoms react to hydroxide (and then to water) rather than to carbon monoxide, because for the latter reaction the carbon atom has to split all bonds with hydrogen. For a high catalyst loading (low *CSV*) it is more likely that the adsorbed oxygen reacts with carbon atoms to form carbon monoxide and carbon dioxide, because its splitting reaction is faster. Thus, the hydrogen atoms that remain from the methane molecule can connect to form hydrogen H_2(s) that eventually desorbs. Hence, the lower the *CSV*, the higher the hydrogen yield in the oxygen rich region. Farther downstream, in the oxygen deficient region, hydrogen production is also influenced by the adsorption and splitting of water on the catalyst

surface. Again, the oxygen inside the water molecule has to release both hydrogen atoms in order to react with a carbon atom. The lower the number of active sites (high *CSV*), the faster the splitting of both water and methane leading to higher hydrogen yield. Hence, variation of *CSV* leads to a change of hydrogen selectivity, which is at a maximum for the lowest *CSV* = 0.6×10^6 m^3 $kmol^{-1}$ s^{-1} (ζ_{H2} = 85.5%) and at a minimum for the highest *CSV* = 3.7×10^6 m^3 $kmol^{-1}$ s^{-1} (ζ_{H2} = 60.2%). Thus, the chemistry changes with different amounts of catalyst. The amount of catalyst represented by *CSV* has a stronger influence on hydrogen yield than on methane conversion.

2.1.2 Constant CSV, variable GSV

The influence of GSV on the reforming process of methane has been investigated in a previous study by changing the inlet velocity at constant geometry and constant amount of catalyst [8]. However, by doing so, the CSV changes as well. In this study, the GSV is also varied by altering the inlet velocity and by leaving the reactor geometry constant. At the same time, the catalyst density is adjusted in order to obtain a constant CSV = 9.19×10^5 m^3 $kmol^{-1}$ s^{-1}. The inlet velocity changes from 0.44 m s^{-1} to 2.25 m s^{-1} corresponding to a GSV of 44.4 s^{-1} and 225 s^{-1}, respectively. The flow is still in the laminar regime, since the inlet Reynolds number does not exceed 25. The corresponding amount of catalyst is $n_{cat} = 0.4 \times 10^{-12}$ kmol for a GSV = 44.4 s^{-1} and $n_{cat} = 1.9 \times 10^{-12}$ kmol for a GSV = 225 s^{-1}. The higher the GSV the higher the amount of catalyst in order to balance the CSV. The diameter of the channel is constant (d = 1 mm).

Right behind the inlet, the methane conversion is monotonic with respect to GSV (Fig. 10a): the higher the GSV the lower the methane conversion.

Fig. 10: *(a) Methane conversion and (b) hydrogen yield along the channel for different GSV at a constant CSV = 9.19×10^5 m^3 $kmol^{-1}$ s^{-1}.*

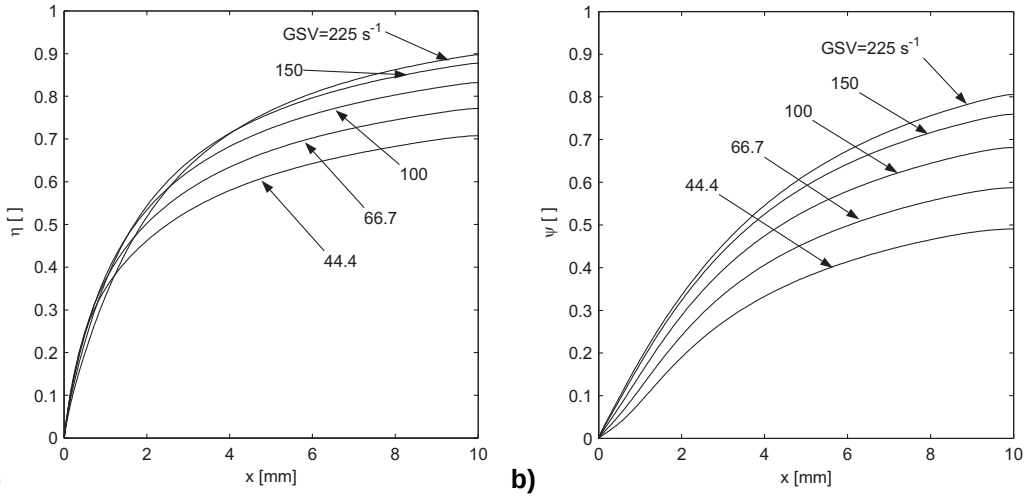

Farther downstream this trend is reversed. The higher the GSV the higher the methane conversion. To this end, two competing processes influence methane conversion. The first is the gas-phase diffusion in the flow channel, the second is the adsorption and reaction of methane on the catalyst surface. Gas phase diffusive resistance is responsible for the low methane conversion right behind the inlet if the GSV is high. The residence time inside the reactor is short for high GSV. Hence, the time period for the components to diffuse to the wall is short. In the second monotonic region the high catalyst surface density has to be responsible for the high methane conversion for the models with a high GSV. The influence of the catalytic surface site density on the splitting process of methane has already been discussed. The highest methane conversion (η = 89.7%) is obtained for GSV = 225 s^{-1}, the lowest methane conversion (η = 70.8%) for GSV = 44.4 s^{-1}. Thus the splitting process of methane, which is fast if the amount of catalyst is high, becomes more and more dominant downstream and counteracts the effect of diffusive resistance.

Hydrogen yield is monotonic with respect to GSV for all cases considered in this study at every axial position (Fig. 10b): the higher the GSV the higher the hydrogen yield. The highest hydrogen yield (ψ =

80.6%) is calculated for GSV = 225 s^{-1}, the lowest hydrogen yield (ψ = 49.0%) for GSV = 44.4 s^{-1}. The difference between maximum and minimum hydrogen yield ($\Delta\psi$ = 31.6%) is significantly higher than that between maximum and minimum methane conversion ($\Delta\eta$ = 18.9%). Hence, variation of the GSV affects the hydrogen selectivity, which is highest for the highest GSV = 225 s^{-1} (ζ_{H2} = 89.8%) and lowest for the lowest GSV = 225 s^{-1} (ζ_{H2} = 69.3%). Therefore, the reaction path is strongly affected by the variation of GSV. In a previous study, a lowering of methane conversion and hydrogen yield was reported for an increasing GSV because the CSV was not considered [8]. But if CSV is held constant, this study clearly shows that both the methane conversion and the hydrogen yield increase, if the GSV is increased. The reason for this outcome is discussed below, by studying the behavior of the temperature and the mole fractions of the individual components at the channel wall.

The temperature at the channel wall is plotted for different GSV in Fig. 11.

Fig. 11: *Temperature at the channel wall along the channel for different GSV at a constant CSV = 9.19x10^5 m^3 $kmol^{-1}$ s^{-1}.*

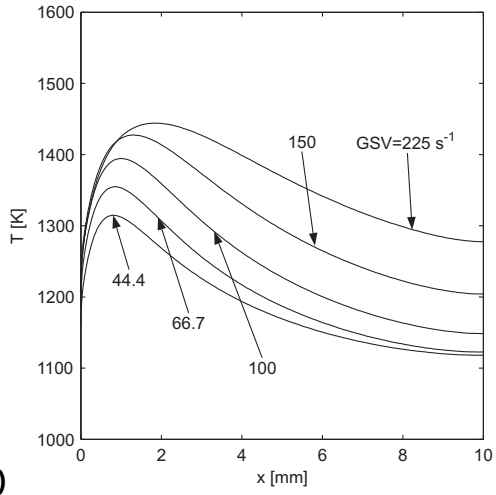

a)

The higher the GSV the higher the maximum temperature. The maximum temperature (T = 1444 K) for GSV = 225 s^{-1} is located at x = 1.9 mm; that for the GSV = 44.4 s^{-1} (T = 1315) lies at x = 0.8 mm. Therefore the higher the GSV, the higher the exothermicity near the inlet. This result stands in contrast to that in the previous section of constant GSV. In the case of constant CSV high methane conversion and high hydrogen yield are obtained if the wall temperature is high. The oxygen mole fraction at the channel wall is plotted for different GSV values (Fig. 12a).

It is clearly visible that the higher the GSV, the more delayed the onset of the oxygen deficient region. Therefore the area, where oxidative reactions are responsible for heat release, is large if the GSV is high. This explains the different locations of maximum wall temperature for a variable GSV (Fig. 11). The onset of the oxygen deficient region is the earliest (x = 1.7 mm) for GSV = 44.4 s^{-1} and the latest (x = 5.0 mm) for GSV = 225 s^{-1}. Thus, the results in the first section are confirmed; oxygen adsorption is mainly limited by gas phase diffusion in the flow channel. It is hardly influenced by the amount of catalytically active sites.

An unexpected outcome is the fact that the value of maximum temperature is high for high GSV (Fig. 11), although the oxygen conversion near the inlet is low. A high oxygen consumption normally implies a high activity of exothermic oxygen consuming reactions. This behavior can be explained by the volumetric flow rate that is higher if the GSV is increased. Therefore the inlet mole flow of methane is higher, and so is the molar amount of methane that can be converted per time unit.

In Fig. 12b it is visible that the lower the GSV, the higher the maximum amount of water. This is a result of the fact that the water producing reactions COG and TOX use oxygen as a reactant and the oxygen conversion is high near the inlet if the GSV is low. Thus, the low volume flow rate compensates for the high exothermic nature of the reactions leading to an overall low temperature (Fig. 11). Water consumption, which is the difference between the maximum water mole fraction and the outlet mole fraction at the channel wall, is an indicator of the strength of SR. Water consumption is the lowest (Δx_{H2O} = 6.5 %) for the highest GSV and the highest for a GSV = 66.7 s^{-1} (Δx_{H2O} = 8.1 %). Although the activity of SR is low, the hydrogen yield has still the highest value when the GSV is high (Fig. 10b).

Fig. 12: *(a) Oxygen, (b) water, (c) carbon monoxide, and (d) carbon dioxide mole fraction at the channel wall along the channel for different GSV at a constant CSV = 9.19x10^5 m^3 kmol^{-1} s^{-1}.*

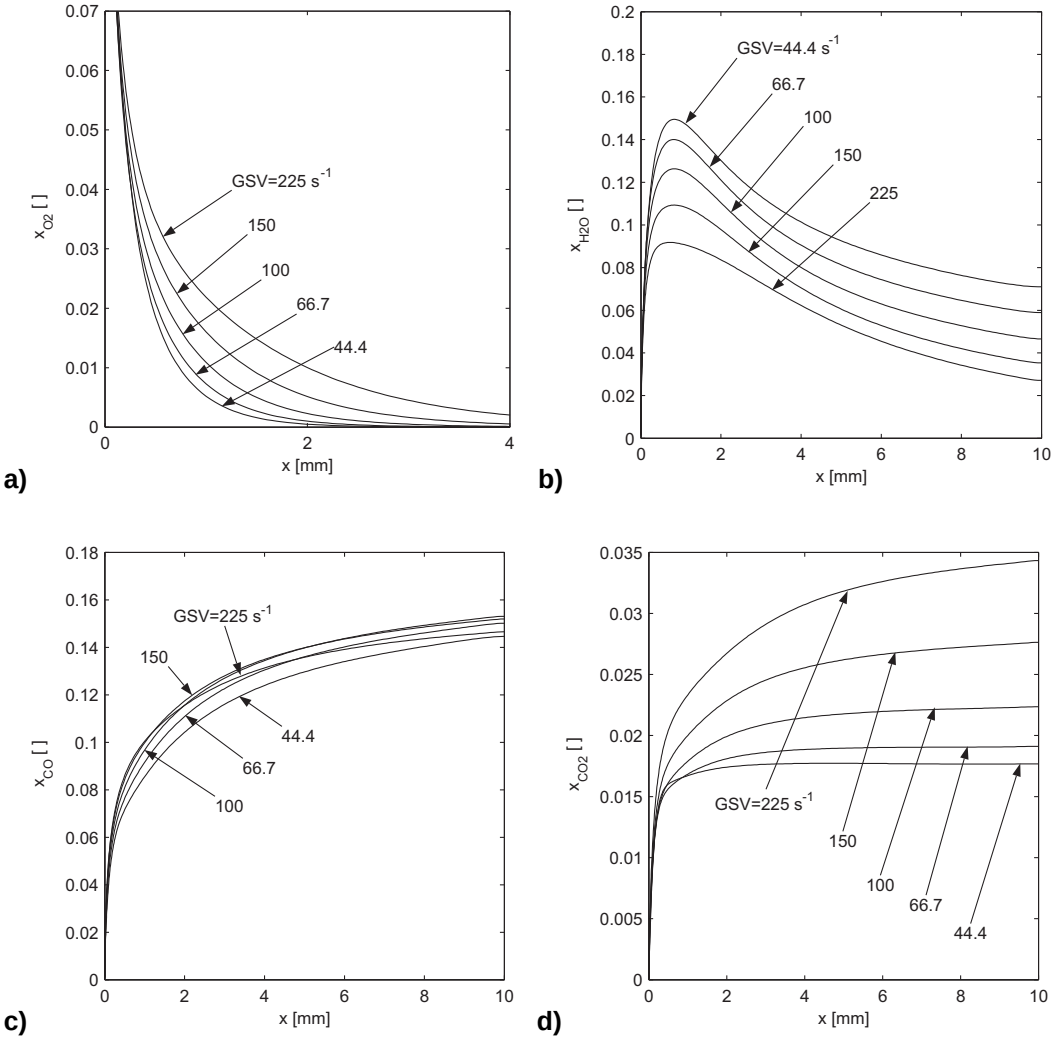

The carbon monoxide mole fraction at the channel wall shows a non-monotonic behavior with respect to GSV. Only directly behind the inlet (x < 1 mm) the dependence on GSV is monotonic: the higher the GSV the higher the carbon monoxide mole fraction. In the previous section, where GSV has been kept constant, the results have shown a high carbon monoxide mole fraction (Fig. 9c) for the same conditions that also have a high hydrogen yield (Fig. 7b). This is not true for the cases where CSV is kept constant. Near the inlet (x < 1 mm) mainly COG and POX are responsible for carbon monoxide production. From the water mole fraction at the channel wall it is deduced that the higher the GSV the lower the COG, that produces both water and carbon monoxide. Because carbon monoxide mole fraction is high for high GSV, the other carbon monoxide producing mechanism, namely POX, has to compensate for the weak COG. Therefore the high hydrogen yield (Fig. 10b) for high GSV at the inlet is mainly due to strong POX, although methane conversion (Fig. 10a) is low. Farther downstream (x > 1 mm) the carbon monoxide mole fraction is not monotonic with respect to the GSV anymore. Hence, a carbon monoxide consuming reaction has to be active for the models with a high GSV. Both the OXCO and the WGS consume carbon monoxide and they both produce carbon dioxide. Yet it was shown that WGS can be neglected in methane reforming reaction on rhodium [11]. Therefore, the carbon dioxide mole fraction at the channel wall is of interest to study the activity of OXCO.

After a non-monotonic region behind the inlet, the carbon dioxide mole fraction becomes monotonic with respect to the GSV (Fig. 12d): the higher the GSV, thus the higher the catalytic surface site density, the higher the carbon monoxide mole fraction (if the GSV is low the OXCO is weak).

It can be concluded that the higher the GSV the higher the hydrogen yield, due to a favoring of POX to COG, which means that methane is converted to hydrogen rather than to water and faster methane conversion occurs for a larger amount of catalyst.

2.1.3 Constant GSV, constant CSV

Next, the influence of the reactor geometry represented by the reactor diameter on the reformer performance is analyzed for a constant *GSV* = 100 s^{-1} and a constant *CSV* = 9.19x10^{5} m^{3} $kmol^{-1}$ s^{-1}. The reactor diameter is changed from *d* = 0.67 mm to *d* = 3.0 mm and the corresponding amount of catalyst varies from n_{cat} = 0.38x10^{-12} kmol to n_{cat} = 7.69x10^{-12} kmol to obtain a constant *CSV*. The reactor length *l* = 10 mm and the inlet velocity u_{in} = 1.0 m s^{-1} are constant, meaning that the catalytic surface area is proportional to the channel diameter. By rewriting Eq. (5) it follows that the amount of catalyst n_{cat}, represented by the number of exposed active catalyst sites (Rhodium) on the catalytically active interface between channel and wall, is a quadratic function of the channel diameter whereas the catalyst density is only a linear function of the same. The flow is in the laminar regime, since the inlet Reynolds number varies between 7 and 31.

Methane conversion along the reformer channel is shown for different reactor diameters in Fig. 13a.

Fig. 13: *(a) Methane conversion, (b) methane mole fraction at the channel wall, (c) hydrogen yield, and (d) hydrogen mole fraction at the channel wall for different channel diameters at a constant CSV = 9.19x10^{5} m^{3} $kmol^{-1}$ s^{-1} and a constant GSV = 100 s^{-1}.*

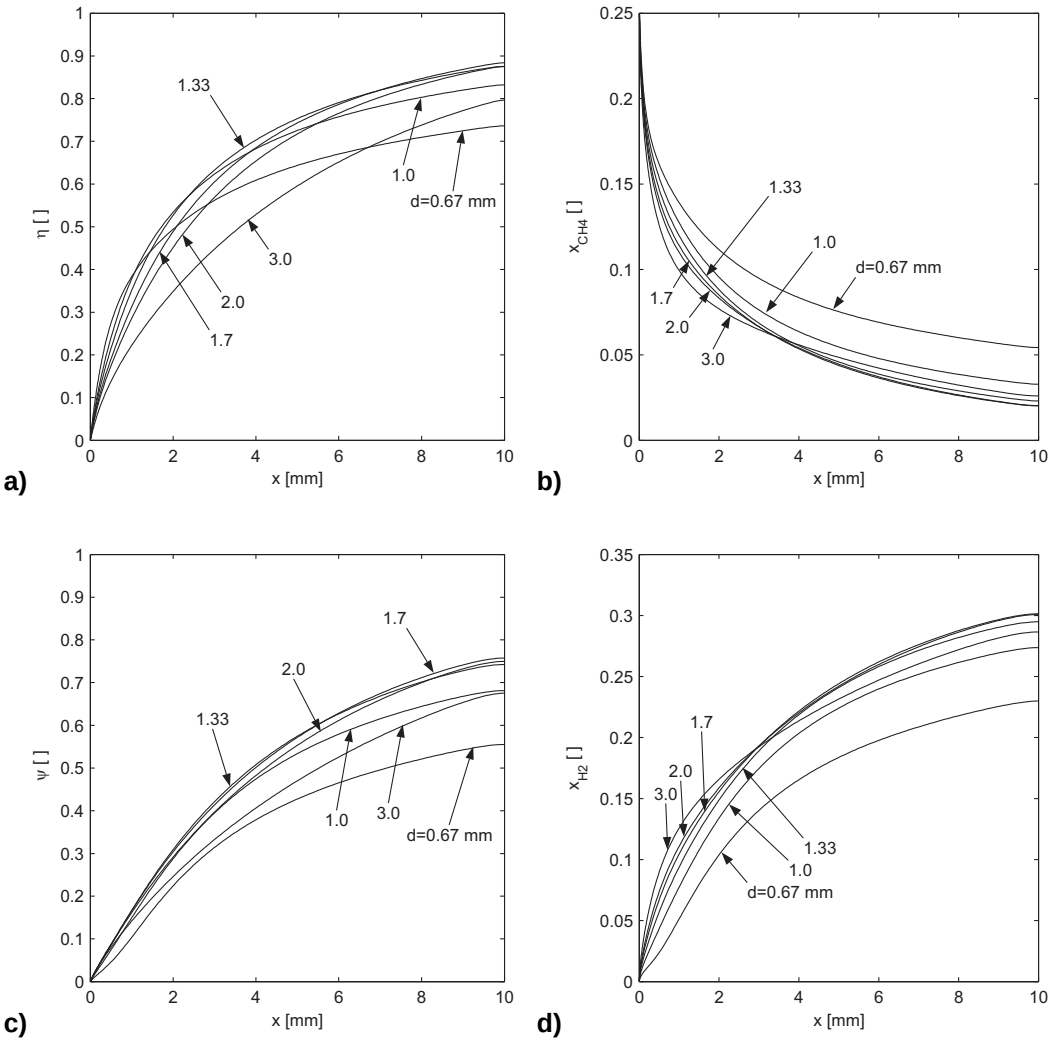

Only very close to the inlet the methane conversion shows a monotonic behavior depending on the channel diameter. The smaller the diameter, the shorter the distance to cover and thus the faster the transport of all components to feed the adsorption mechanisms. This leads to a higher methane conversion. However, by studying the methane mole fraction at the channel wall (Fig. 13b) it is visible that the methane mole fraction is high for a small diameter. Thus, the adsorption rate of methane itself is low for a small channel diameter because the catalytic surface area is smaller and the catalytically active surface site density is low. It appears that two competing mechanisms, the species transport

and the adsorption mechanism, affect the methane conversion and are responsible for its non-monotonic behavior farther downstream.

It is worth noting that in this section, where the channel diameter is varied, both the radially averaged mole fractions (including methane conversion and hydrogen yield) and the mole fractions at the channel wall need to be studied. The species mole fractions at the channel wall provide information about the activity of the surface reaction mechanisms. Together with the mean mole fractions the species transport mechanism can be reproduced.

The hydrogen yield is non-monotonic along the channel with respect to the channel diameter (Fig. 13c), even close to the inlet, where the hydrogen mole fraction at the channel wall is monotonic (Fig. 13d). The transport mechanism, which is enhanced if the diameter is lowered, competes with the reaction rate on the surface that is stronger if the diameter is enlarged. Hydrogen selectivity is lowest (ζ_{H2} = 75.4%) for the smallest diameter d = 0.67 mm and shows a maximum (ζ_{H2} = 85.7%) for d = 1.7 mm. The largest diameter (d = 3.0 mm) still has a rather high hydrogen selectivity (ζ_{H2} = 84.8%). Even if the two characteristic values *CSV* and *GSV* are held constant, the chemical reactions vary significantly.

Neither the value of maximum wall temperature nor its position shows a monotonic behavior with respect to the channel diameter (Fig. 14a).

Fig. 14: *(a) Temperature and (b) oxygen mole fraction at the channel wall along the channel for different channel diameters at a constant CSV = 9.19x10^5 m^3 kmol^{-1} s^{-1} and a constant GSV = 100 s^{-1}.*

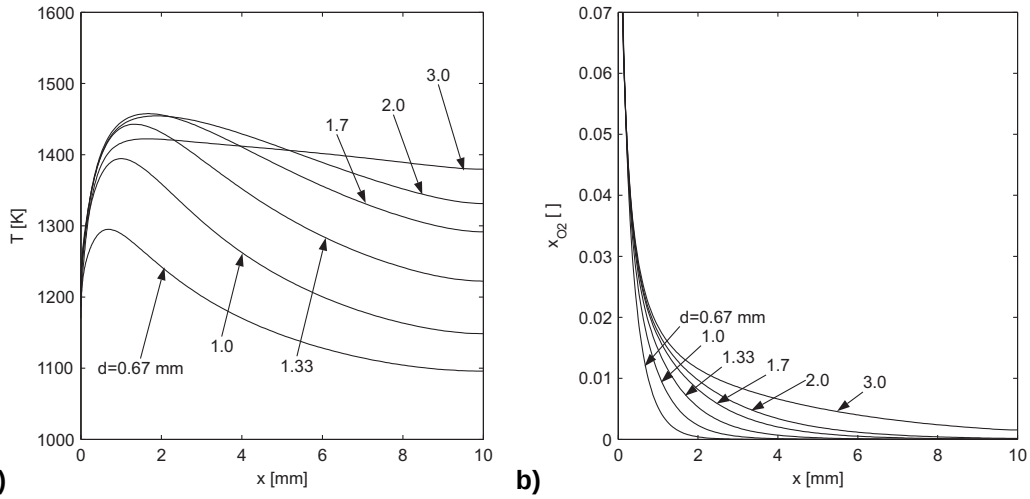

This is again due to the competing effects of species transport and adsorption/reaction rate. The highest maximum wall temperature (1457.5 K) is obtained for the model with a reactor diameter d = 1.7 mm. Therefore, the highest maximum wall temperature, the maximum methane conversion, and the maximum hydrogen yield are reached for the same diameter d = 1.7 mm. After the location of the wall temperature peak, the endothermic reactions, especially SR, are responsible for the monotonic decrease of wall temperature in the axial direction [11]. One indicator of the activity of SR is the temperature drop behind the peak. It strongly depends on the channel diameter. For the smallest diameter d = 0.67 mm, the difference between the maximum and the outlet temperatures amounts to 199 K and for d = 1.0 mm, the highest temperature difference (ΔT = 246 K) occurs. Larger diameters result in lower temperature differences: the temperature difference for d = 3.0 mm is only 43 K implying weak SR.

The oxygen mole fraction at the channel wall is monotonic regarding the channel diameter all along the channel (Fig. 14b). The larger the channel diameter, the higher the oxygen mole fraction. The length of the oxygen deficient region decreases significantly with increasing channel diameter: for a diameter d = 0.67 mm, the oxygen deficient region starts at x = 1.6 mm, whereas for d = 3.0 mm, there is no oxygen deficient region at all. In this case, the outlet oxygen mole fraction at the wall is still 0.15%. This result agrees well with the previous findings herein: the oxygen consumption is mostly determined by gas phase diffusion in the channel and is hardly effected by the catalyst amount. If the channel diameter is increased, the oxygen rich region is enlarged. Thus, exothermic oxygen

consuming reactions can heat up a larger area of the reactor leading to a higher temperature near the outlet (Fig. 14a).

To compare the activity of SR of the different cases the radially averaged water mole fraction along the centerline is investigated (Fig. 15a).

Fig. 15: *(a) Radially averaged water, (b) carbon monoxide, and (c) carbon dioxide mole fraction along the channel for different channel diameters at a constant CSV = 9.19x10^5 m^3 kmol^{-1} s^{-1} and a constant GSV = 100 s^{-1}.*

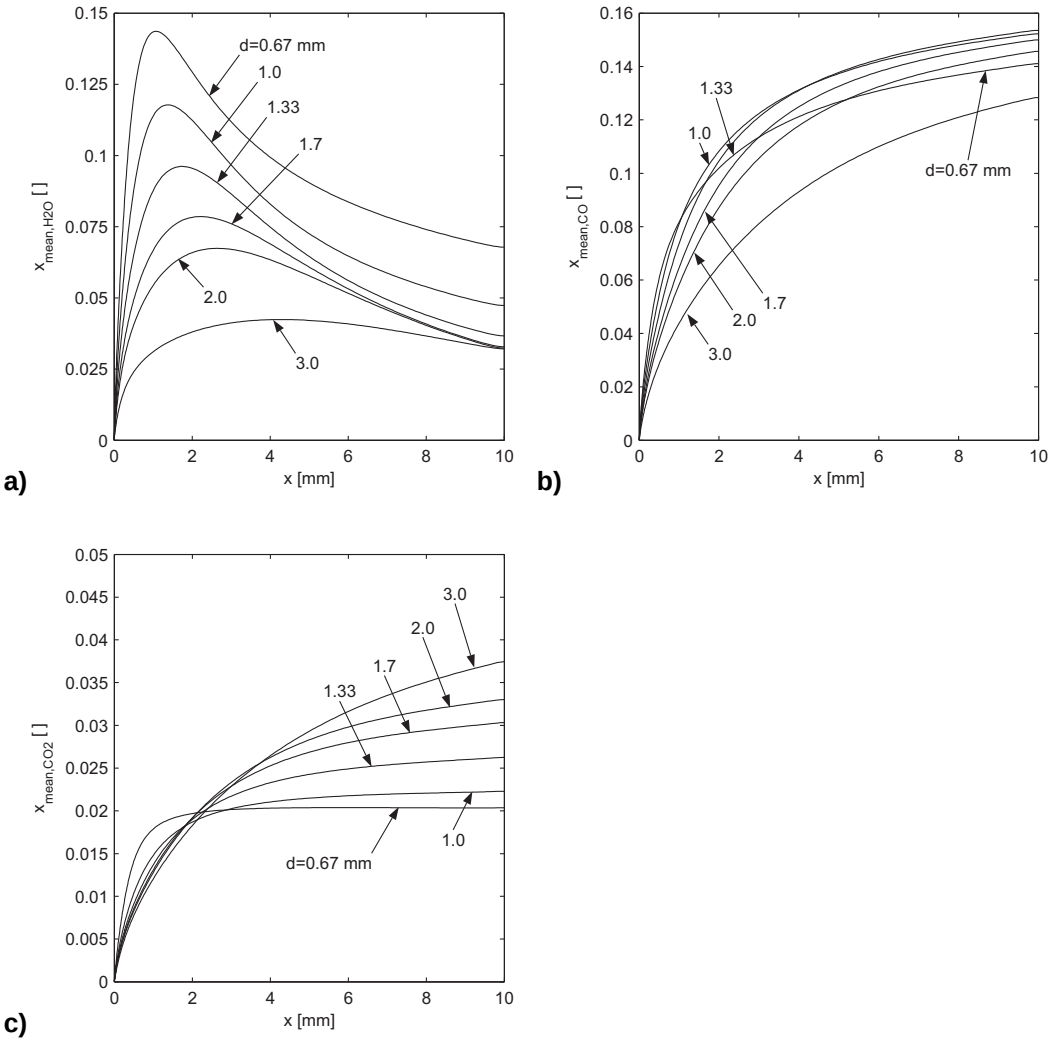

By using the mean value of water mole fraction the activity of SR cannot be spacially resolved but it can be better globally quantified because the radial concentration gradients are included. A monotonic behavior with respect to the channel diameter is exhibited. The smaller the channel diameter, the higher the mean water mole fraction. The maximum value (x_{H2O} = 14.4%, for d = 0.67 mm) is more than three times larger than for d = 3.0 mm (x_{H2O} = 4.2%). This result corresponds well to the earlier findings herein: The higher the catalyst density on the surface the faster the decomposition of methane, hence the lower the water production. This effect is enhanced by the oxygen transport process, which is slower if the diameter is increased. Therefore, there is less oxygen on the surface to support the water producing and oxygen consuming TOX and COG. The difference between maximum and outlet water mole fraction is another indicator of the activity of SR. The results confirm those obtained for the wall temperature (Fig. 14a). The difference in water mole fraction is highest (Δx_{H2O} = 7.6%) for d = 0.67 mm, whereas the difference in mole fraction for d = 3.0 mm is only Δx_{H2O} = 1.0% indicating low activity of SR.

Close to the inlet, the radially averaged carbon monoxide mole fraction increases monotonically with decreasing channel diameter (Fig. 15b). Carbon monoxide is mainly produced by oxygen consuming

reactions (POX and COG). Hence, the fast oxygen transport in channels with small diameters is responsible for the high carbon monoxide production. Farther downstream, the dependence of the mean carbon monoxide mole fraction on the diameter is not monotonic anymore, due to the low production rate for channels with a small diameter. Thus, there are again two competing effects that influence the carbon monoxide production: the first is the activity of SR that is high for small diameters. The second is the surface site density, which lowers methane conversion if the diameter is decreased, meaning that less carbon atoms are present to be converted to carbon monoxide, leading to a decrease of carbon monoxide production.

Right after the inlet, the mean carbon dioxide mole fraction is monotonic with respect to the channel diameter (Fig. 15c): the lower the channel diameter the faster the oxygen transport inside the channel, hence the higher the carbon dioxide production. Farther downstream, there is again a monotonic behavior, following however the opposite trend. It has been shown earlier that a low catalyst density leads to a low carbon dioxide production. Close to the inlet, the effect of species transport is dominant yielding a high carbon dioxide mole fraction for a small diameter. Farther downstream, the low catalyst density is responsible for the low carbon dioxide mole fraction for a small diameter.

Both the species transport and the properties of the catalytically active surface significantly affect the reactor performance. Increasing the channel diameter raises the diffusive resistance but enlarges the surface area. Increasing the catalytic surface site density changes the activity of the diverse surface reactions resulting in an alteration of the selectivities. This enforces the necessity of coordinating the channel diameter selection, the inlet volume flow rate, and the catalyst amount to obtain an optimal reformer performance. The optimum performance for the parameters investigated herein is obtained for a diameter d = 1.7 mm, corresponding to a catalyst amount n_{cat} = 2.5x10^{-12} kmol, where hydrogen yield exhibits a maximum (ψ = 75.7%) at the outlet (Fig. 16).

Fig. 16: *Methane conversion η and hydrogen yield ψ at the channel outlet for different channel diameters at a constant CSV = 9.19x10^5 m^3 kmol^{-1} s^{-1} and a constant GSV = 100 s^{-1}.*

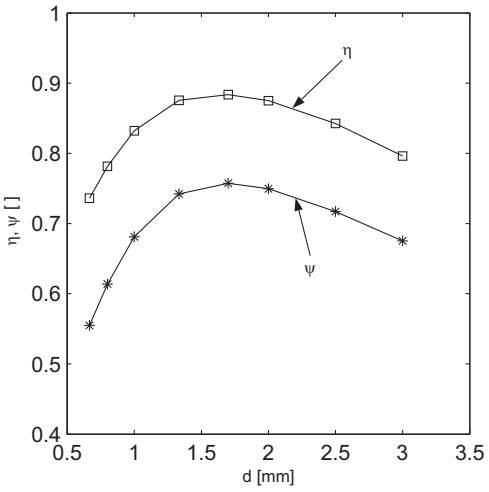

For the same diameter the methane conversion (η = 88.4%) exhibits a maximum as well. This result is significant because it implies that there is an optimum diameter and therefore an optimum amount of catalyst for the highest hydrogen yield and methane conversion. Hence, increasing the amount of catalyst does not automatically enhance the reforming performance.

Therefore mass transfer is not the limiting factor in butane reforming. Analytical calculations of the diffusive length of butane in air underline this outcome. The diffusive length inside the reformer is approximated as a steady state point source of butane in a uniform stream of air [19] at 600℃ and reads

$$l_{diff} = \sqrt{4\,D\,t} = 1.9\,mm \qquad (6)$$

with the diffusion coefficient of butane in air as D = 8.91x10^{-5} m^{2}s^{-1} and the space time t = 10 ms describing the ratio of the channel length to the inlet velocity. This calculation shows that the radius of the reformer is significantly smaller than the diffusion length. Thus, the diffusive mass transport is fast enough to and not limiting to the reforming activity of butane.

2.2 CONCLUSIONS

The effects of catalyst surface site density, representing the catalyst amount, and reactor diameter on the reforming process of methane in a wall-coated, single-channel microreactor have been investigated numerically. The radially symmetric numerical domain consists of two subdomains, the flow channel and the thermally conductive channel wall. At the interface an elementary surface reaction mechanism describing methane reforming on rhodium catalyst is applied. The outer boundaries are adiabatic due to symmetry conditions in a monolith.

It is found that catalyst loading strongly influences the reactor performance. The higher the catalyst surface site density the higher the hydrogen yield and the methane conversion for a constant *GSV* and reactor geometry. An unexpected result is the significant change of hydrogen selectivity with varying *CSV*, meaning that the chemistry changes with varying catalyst loading. A high catalyst density enhances hydrogen production in the oxygen rich region due to the fast splitting of the adsorbed methane on the surface. In the oxygen deficiency region, a high catalyst density enhances water splitting, which is the limiting factor in SR, leading again to a higher hydrogen production.

If the *CSV* and the reactor geometry are kept constant, increasing the *GSV* leads again to a significant increase of hydrogen selectivity. This means that different reaction routes are dominant for different *GSV*. In this case, the higher hydrogen yield and methane conversion for increasing *GSV* is due to a favoring of hydrogen producing POX than to water producing COG. This is the result of the faster decomposition of methane on the catalytic surface. Furthermore, the wall temperature increases significantly by raising *GSV*. This is due to the increase of the inlet volumetric flow rate, thus the amount of methane that can be converted.

Furthermore, the reforming process is investigated by keeping both *CSV* and *GSV* constant, and varying the channel diameter. An optimum configuration is found with an optimum amount of catalyst and channel diameter, which is an unexpected result. Thus, enhancing the amount of catalyst and/or decreasing the channel diameter do not automatically increase the reactor performance. Moreover it can even lower it. As a consequence, it is expected that the implementation of a tree network structure does not enhance the reforming performance markedly since the mass transfer is not the limiting factor.

This enforces the necessity of coordinating the selection of channel diameter, inlet volume flow rate, and catalyst amount to obtain maximum reformer performance. Additionally, it is worth noting that the amount of catalyst in a catalytic reactor is not sufficiently characterized by the *CSV* alone, and it is not sufficient that the flow condition is only characterized by the *GSV*. In order to characterize a catalytic reactor sufficiently, the declaration of all the *CSV*, *GSV* and geometry is absolutely necessary.

3. Experimental investigation of butane-to-syngas reforming

The capability of flame-made $Rh/Ce_{0.5}Zr_{0.5}O_2$ nanoparticles catalyzing the reforming of butane to H_2- and CO-rich syngas was investigated for different Rh loadings (0.1 – 2.0 wt% Rh) and two different ceramic fibers (Al_2O_3/SiO_2 and SiO_2) as plugging material in a packed bed reactor for a temperature range from 225 to 750℃. The main goal of this study was the efficient reforming of butane at temperatures between 500 and 600℃ for a micro intermediate-temperature SOFC system. Our results showed that $Rh/Ce_{0.5}Zr_{0.5}O_2$ nanoparticles offer a very promising material for butane-to-syngas reforming with complete butane conversion and a hydrogen yield of 77% at 600℃. The reforming performance of packed beds strongly depended on the use of either Al_2O_3/SiO_2 or SiO_2 fiber plugs. This unexpected effect could be attributed to the interplay of homogeneous and heterogeneous chemical reactions during the high-temperatures within the reformer.

The major goal of the experimental study was to investigate the feasibility of reforming butane-to-syngas with high H_2 and CO mole fractions at relatively low temperatures, while obeying strict limitations of space considering the application of a micro SOFC system. To achieve these demanding requirements, ceria/zirconia nanoparticles with rhodium doping ($Rh/Ce_{0.5}Zr_{0.5}O_2$) made by flame spray synthesis were used as catalysts. Nanoparticles provide open and easily accessible catalytically active surfaces with a high surface-to-volume ratio, as shown by Stark et al. [20]. Zirconia contributes to the thermal stability of the nanoparticles and ceria offers optimal properties for oxygen exchange on the particle surface [21]. The reforming performance of these nanoparticles was analyzed in a mini packed bed reactor. A preferred reaction path for hydrocarbon reforming is Partial Oxidation (POX), written as

$$C_4H_{10} + 2\,O_2 \rightarrow 5\,H_2 + 4\,CO\,, \qquad (7)$$

which achieves high yields of H_2 and CO and does not need addition of water (H_2O) from an auxiliary tank such as Steam Reforming (SR):

$$C_4H_{10} + 4\,H_2O \rightarrow 9\,H_2 + 4\,CO \qquad (8)$$

or Water Gas Shift (WGS):

$$CO + H_2O \rightarrow H_2 + CO_2 \qquad (9)$$

An efficient reformer should show high selectivity towards POX instead of Total Oxidation (TOX) of butane:

$$C_4H_{10} + 6.5\,O_2 \rightarrow 5\,H_2O + 4\,CO_2\,. \qquad (10)$$

Another objective of this study was the investigation of the effect of different plugging materials of the packed bed on the catalytic performance. Ceramic fibers made of a mixture of silicon oxide and aluminum oxide (SiO_2/Al_2O_3), which is widely used as the sealing material and the substrate of monoliths or foams in hydrocarbon-to-hydrogen reformers, e.g. [22-26], and pure SiO_2 fibers were used to form plugs.

3.1 EXPERIMENTS

$Ce_{0.5}Zr_{0.5}O_2$ nanoparticles with optional rhodium doping were prepared in a one-step process by flame spray synthesis described by Madler et al. and Stark et al. [27, 28]. For the ceria/zirconia precursor, cerium(III) 2-ethylhexanoate (12 wt% Ce, Shepherd Chemical Company) and zirconium(IV) 2-ethylhexanoate (18 wt% Zr, Borchers GmbH) were mixed resulting in a metal molar ratio Ce/Zr of 1:1 and diluted with xylene to a total metal concentration of 0.8 mol L^{-1}. Rhodium(III) 2-ethylhexanoate (UMICORE AG & Co.) was optionally added to the Ce/Zr-precursor such that the calculated rhodium content in the ternary system Rh/ceria/zirconia ($Rh/Ce_{0.5}Zr_{0.5}O_2$) was 2.0, 0.5, 0.25 and 0.1 wt%. The mixtures were fed (5 mL min^{-1}) through a capillary (i.d. 0.4 mm) using a gear-ring pump (HNP Microsysteme) and were dispersed by oxygen at the tip of the capillary (5 L min^{-1}, constant pressure drop at the nozzle 1.5 bar, PanGas, tech) following ignition by a methane (1.13 L min^{-1}, PanGas, tech)/oxygen (2.41 L min^{-1}, PanGas, tech) supporting flame. The burning spray of the flame synthesis reactor was stabilized by a concentric oxygen sheath flow (230 L h^{-1}, PanGas, tech). All gas flows were controlled by calibrated mass flow controllers (Brooks). The particles formed in the flame were separated from the off-gas with a glass fiber filter (Whatman GF/A, 25.7 cm in diameter) placed above the flame by the aid of a vacuum pump (Busch Seco SV 1040 C). The thermal stability was tested by sintering as prepared particles at 1000℃ for 16 h, under air, using a heating rate of 10℃ min^{-1} and measuring the remaining specific surface area.

Fig. 17: *Schematic of the test setup for catalyst performance measurements of a packed bed reactor*

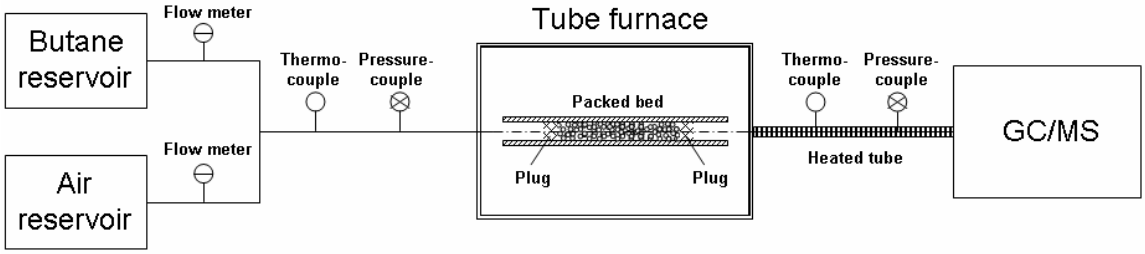

The experimental test setup to measure the catalyst performance is shown in Fig. 17. Expanded butane from a liquid tank (PanGas, 3.5) at 2.5 bar was mixed with compressed synthetic air (79% N_2, 21% O_2, PanGas, 5.6) from a gas tank (Fig. 17). Both flow rates were controlled by Low Delta-P flow meters (Bronckhorst). The flow meters allowed control of the inlet pressure to reach the ambient pressure at the system outlet and therefore to operate the reactor slightly above ambient pressure. The butane/air mixture was fed into a packed bed reactor inside an Inconel tube (Alloy 600, i.d. 2 mm) and heated by a tube furnace (MTF 12/38/250, Carbolite). The tube was heated over a length of 30 cm, ensuring isothermal conditions along the packed bed reactor (total length: 11 mm) placed in the middle of the furnace. The product gas leaving the furnace through an Inconel tube was maintained at around 115℃ to avoid condensation of H_2O. The gas composition was analyzed by a gas chromatograph (6890 GC) coupled with a mass spectrometer (5975 MS, Agilent), using a HP-MOLSIV and a HP-PlotQ column (Agilent), respectively. Helium (PanGas, 5.6) was added as an internal standard for GC calibration. Under typical run conditions, the molar product gas balances of carbon (C), hydrogen (H) and oxygen (O) were closed within 5%.

The packed bed consisted of 22.5 mg purified and calcined SiO_2 sand (Riedel-deHaën, average diameter: 0.2 mm) and 7.5 mg $Rh/Ce_{0.5}Zr_{0.5}O_2$ nanoparticles, prepared as shown before and homogenously distributed onto the sand particles. For reference measurements without catalyst, packed beds with 30.0 mg SiO_2 were prepared. These porous packed beds were fixed in the Inconel tube between ceramic fiber plugs, as shown in Fig. 17. In order to investigate the reactivity of the fibers, two different ceramic materials were used: Ceramic fiber paper made of SiO_2 and Al_2O_3 (1:1, CT 1260 P, Contherm, mean fiber diameter: approximately 18 µm, mean fiber length: 5 mm) or pure SiO_2 fibers (Riedel-deHaën, mean fiber diameter: 16 µm, mean fiber length: 5 mm).

The activity of $Rh/Ce_{0.5}Zr_{0.5}O_2$ catalyst was tested at constant air and butane inlet flow rates of 15.0 and 1.2 ml min^{-1}, respectively, leading to mole fractions of X_{C4H10} = 7.4%, X_{O2} = 18.5% and X_{N2} = 74.1%. This corresponded to a butane mass flow of 0.2 g h^{-1}. The C/O ratio or equivalence ratio ϕ based on POX was defined based on the molar flow $\dot{n}_i$ as

$$\phi = 2 \cdot \frac{\dot{n}_{C_4H_{10},in}}{\dot{n}_{O_2,in}} \tag{11}$$

and was kept constant at ϕ = 0.8 for all measurements, as suggested by previous numerical studies on micro hydrocarbon reformers [8, 11]. The entire reactor was heated from 225℃ to 750℃ at a heating rate of 2.5℃ min^{-1} under air/butane flow. The molar composition of the outlet gas was determined every 75℃. The mean gas velocity at the reactor inlet varied from 0.14 to 0.29 m s^{-1}, depending on the reactor temperature, leading to *GSV* between 15.7 and 32.3 s^{-1} and t_{space} in the range of 63.7 and 31.0 ms. Based on the results of the GC/MS, the butane conversion η of the micro reformer was determined as the molar ratio between converted butane and inlet butane:

$$\eta = \frac{\dot{n}_{C_4H_{10},in} - \dot{n}_{C_4H_{10},out}}{\dot{n}_{C_4H_{10},in}} \tag{12}$$

The hydrogen yield was defined as the molar ratio of H_2 in the outlet gas and the maximal possible amount of H_2 formed at full conversion according to Eq. (7):

$$\psi = \frac{\dot{n}_{H_2,out}}{5 \cdot \dot{n}_{C_4H_{10},in}} \tag{13}$$

The selectivities for H_2 and CO were defined as:

$$S_{H_2} = \frac{\dot{n}_{H_2,out}}{\dot{n}_{H_2,out} + \dot{n}_{H_2O,out}} \quad (14)$$

and

$$S_{CO} = \frac{\dot{n}_{CO,out}}{\dot{n}_{CO,out} + \dot{n}_{CO_2,out}} . \quad (15)$$

3.2 RESULTS

3.2.1 Reforming performance with Al_2O_3/SiO_2 fibers

In Fig. 18, the resulting reforming performance of packed bed reactors containing Al_2O_3/SiO_2 fiber plugs is shown. For a packed bed reactor consisting of SiO_2 sand without any $Rh/Ce_{0.5}Zr_{0.5}O_2$ catalyst, the conversion of butane started above 400℃ (Fig. 18a) slightly increasing to a very low butane conversion η at 600℃. Above 600℃, the butane conversion rose rapidly to 47% at 750℃. However, no H_2 and only a small amount of CO (X_{CO} = 2% at 600℃) were produced in such a reactor without catalyst.

By adding $Rh/Ce_{0.5}Zr_{0.5}O_2$ nanoparticles with 0.5 wt% Rh, conversion of butane started below 300℃ (Fig. 18a). At 300℃, 48% of the butane was converted and after stagnation in butane conversion (at around 50%) up to 525℃, η increased to 96% at 750℃. The H_2 production grew with increasing reactor temperature up to 375℃, stagnated between 375 and 500℃ and finally increased again for temperatures up to 750℃. First, the hydrogen yield ψ rose to 24% at 375℃ (Fig. 18b) and then to 77% at 750℃. Similarly, the H_2 selectivity S_H stagnated at 46% between 375 and 500℃ and reached 84% at 750℃ (Fig. 18d). The CO production slowly increased up to 525℃ and rose rapidly for higher temperatures. The CO selectivity S_{CO} amounted to 9% at 375℃ and started to rise significantly from 20% at 525℃ to 77% at 750℃ (Fig. 18c). The corresponding H_2 and CO mole fractions are presented in the appendix.

There were no significant amounts of lower hydrocarbons in the product gas detected (mole fractions below 0.05%), except for some methane with mole fractions below 0.7%. The molar product gas balance of C closed within 1% for all measurements, indicating that no significant carbon deposition took place inside the reactor.

3.2.2 Reforming performance with SiO_2 fibers

For a packed bed reactor consisting of SiO_2 sand and SiO_2 fiber plugs without any $Rh/Ce_{0.5}Zr_{0.5}O_2$ catalyst, the conversion of butane started above 400℃ (Fig. 18a) significantly increasing to a butane conversion η of 24% at 675℃. Above 675℃, the butane conversion rose rapidly to 49% at 750℃. A small amount of H_2 was produced at 750℃ and only little CO above 600 ℃.

For a reactor with $Rh/Ce_{0.5}Zr_{0.5}O_2$ nanoparticles (0.5 wt% Rh), the butane conversion η reached 45% at 300℃ (Fig. 18a). Above 375℃, η increased up to 99% at 750℃. The H_2 production showed a steep rise between 375 and 525℃. The hydrogen yield ψ increased from 16% at 375℃ to 86% at 675℃ (Fig. 18b). Consistently, the H_2 selectivity S_{H_2} rapidly grew to 76% at 525℃, with a slight further increase to 85% at 750℃ (Fig. 18d). The CO production started above 300℃ and rose rapidly to a CO selectivity S_{CO} of 73% at 675℃ and 79% at 750℃ (Fig. 18c). In the appendix, the resulting H_2 and CO mole fractions are shown.

For the measurements with SiO_2 fiber plugs, the molar product gas balance of C closed within 1% for all measurements, indicating no significant carbon deposition in the reactor, while mole fractions of lower hydrocarbon were below 0.05%, except for a mole fraction of methane below 0.3%.

3.2.3 Reforming performance with different Rh loadings

The conversion of butane in packed beds consisting of SiO_2 sand, catalyst nanoparticles with Rh loadings from 2.0 to 0.1 wt% and SiO_2 fiber plugs started below 300℃, where the variation of catalyst loading had no significant influence on the butane conversion η up to 375℃ (Fig. 19a). Between 400

and 600℃, higher Rh loadings led to remarkably higher butane conversion. For the highest Rh loading of 2.0 wt%, η increased rapidly from 56% at 375℃ to 92% at 525° C, reaching complete conversion of butane above 600℃. The difference in conversion for materials with 0.5 and 0.25 wt% Rh was rather small. The addition of 0.1 wt% Rh to the ceria/zirconia had only a minor effect on the butane conversion between 300 and 600℃.

Fig. 18: *(a) Butane conversion η, (b) hydrogen yield ψ, (c) carbon monoxide selectivity S_{CO} and (d) hydrogen selectivity S_{H2} as functions of reactor temperature for packed bed reactors with a catalyst loading of 0.5 wt% Rh and without catalyst and for both types of plugs, with SiO_2 (•) and Al_2O_3/SiO_2 (□) fibers, respectively. The solid lines through the data points are curve fits.*

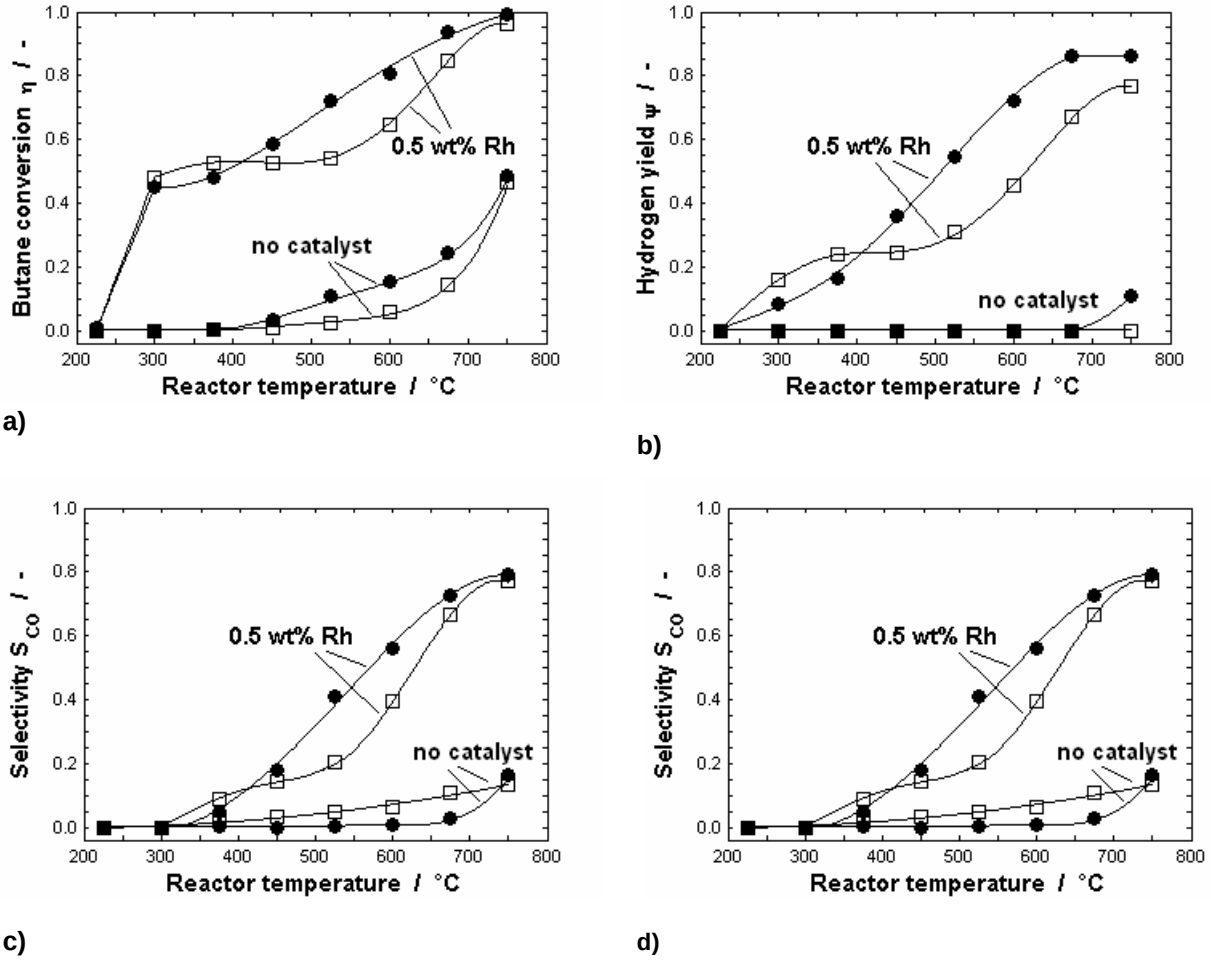

For all investigated materials, the start of butane conversion coincided with the start of H_2 production below 300℃. For 2.0 wt% Rh, the hydrogen yield ψ increased almost linearly to 86% at 675℃, staying at this maximum value for higher temperatures (Fig. 19b). At temperatures below 400℃, the Rh loadings of 0.5 and 0.25 wt% showed nearly the same hydrogen yields. On the other hand, for higher temperatures a catalyst with 0.5 wt% Rh allowed a fast rise in H_2 production. Above 600℃, the addition of more noble metal did not significantly improve the H_2 yield. More specifically for nanoparticles with 0.25 and 0.1 wt% Rh, the hydrogen yield at 750℃ reached 81 and 68%, respectively. For 2.0 wt% Rh, the H_2 selectivity S_{H2} grew rapidly to 75% and reached saturation at 86% above 525℃ (Fig. 19d). For lower catalyst loadings, the H_2 selectivity increased slower in the beginning. Since the H_2 selectivity determined the H_2 mole fraction in the off-gas, the same trend was found for the gas composition.

The production of CO started later than the conversion of butane and the production of H_2, namely above 300℃. Above 400℃, the CO production rose rapidly with large differences in CO selectivity S_{CO} between 500 and 650℃ for different Rh loadings (Fig. 19c). The increase of Rh loading from 0.25 to 0.5 wt% had only a small effect on the CO production. The CO production converged to a maximum of S_{CO} of 83% for all catalyst loadings at 750℃. As in the case of the previous subsection, the off-gases contained below 0.05% of higher hydrocarbons and below 0.9% of methane. The C mass balance was closed within 1%.

Fig. 19: *The influence of Rh loading on $Ce_{0.5}Zr_{0.5}O_2$ on (a) butane conversion η, (b) hydrogen yield ψ, (c) carbon monoxide selectivity S_{CO} and (d) hydrogen selectivity S_{H2}, using plugs of SiO_2 fibers. Bottom: results of a packed bed without catalyst as reference. The solid lines through the data points are curve fits.*

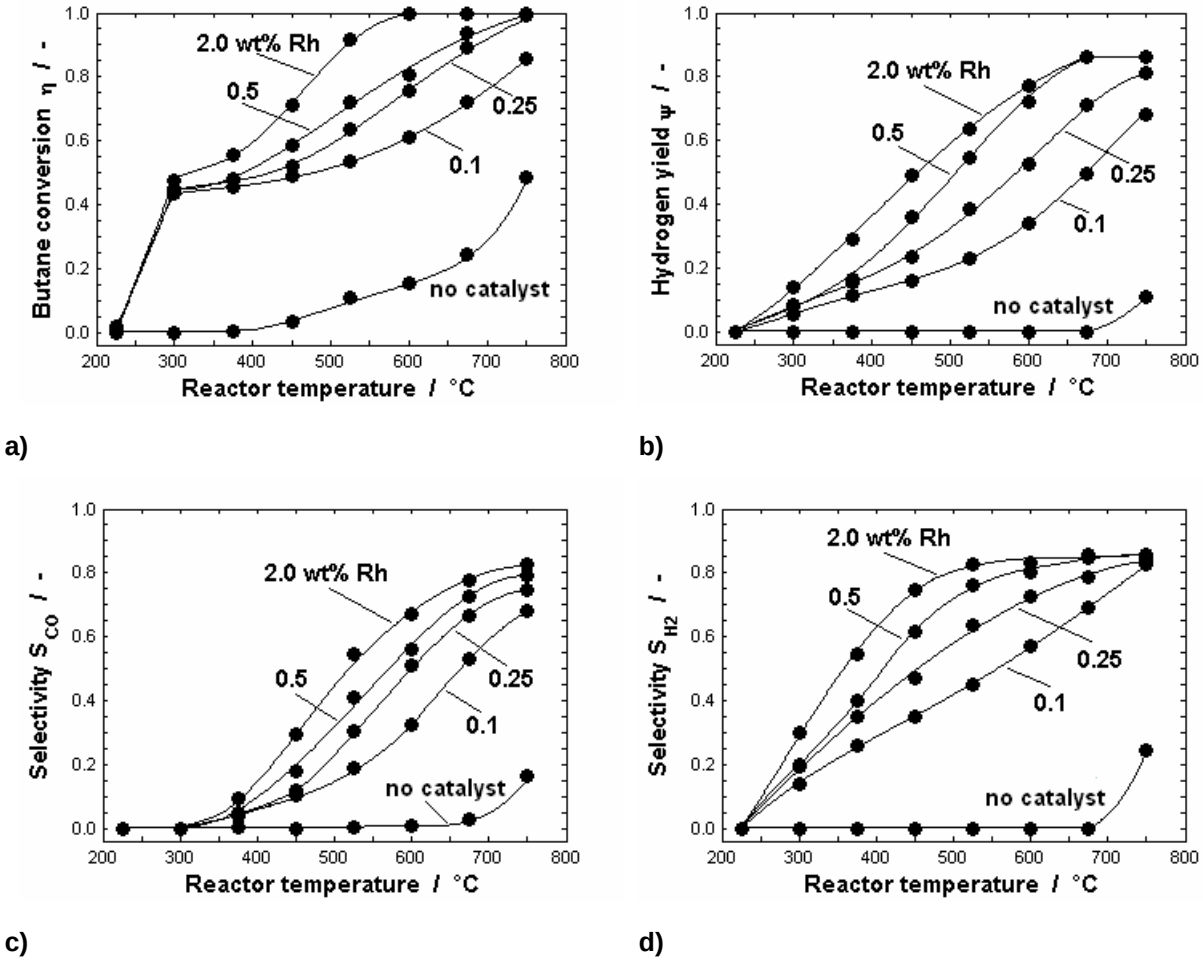

3.3 DISCUSSION

The use of $Rh/Ce_{0.5}Zr_{0.5}O_2$ nanoparticles as catalysts for the Partial Oxidation (POX) of butane allowed production of H_2 and CO at temperatures as low as 300℃. While maximum conversion and highest selectivity to H_2 and CO were found at high temperatures, a satisfactory reforming performance could already be achieved in the present system at relatively low temperatures between 500 and 600℃. This temperature range was suggested for the incorporation in intermediate-temperature SOFC systems [29, 30].

Our more detailed investigation of different reactor materials revealed that the ceramic fiber plugs had a pronounced influence on the overall performance. Fibers consisting of Al_2O_3/SiO_2 resulted in an enhanced butane conversion and H_2/CO production between 300 and 400℃ if compared to pure SiO_2 fibers (Fig. 18). At 400℃, the performance of a SiO_2 fiber based reactor started to exceed those of Al_2O_3/SiO_2 fibers and grew more evident around 500 to 650℃.

In order to analyze this effect, we investigated the reforming process in the absence of any noble metal or ceria-based ceramics and used SiO_2-sand filled tubes with ceramic plugs (Fig. 18). The use of alumina containing fibers significantly reduced the butane conversion by up to a factor of three at 600℃. A closer view on the corresponding hydrogen and CO yields showed that most of the butane is fully oxidized. This clearly illustrated the important contribution of non-noble metal catalyzed butane conversion and possible homogeneous reaction of butane at temperatures above 600℃. At such high temperature, appreciable amounts of butane were obviously reacting without the need of noble metal activation. Other studies [31-33] have suggested in a similar manner that oxidative dehydrogenation of propane is a combination of gas-phase homogeneous and catalyzed heterogeneous reactions, where Xu and Lundsford [33] based this interpretation on experiments with SiO_2 chips comparable to our SiO_2-sand filled tubes. Huff and Schmidt [34] showed that oxidative dehydrogenation of butane in short-time reactors was highly affected by an increase of reactor surface in the absence of noble metal

catalysts. Lemonidou and Stambouli [35] confirmed this effect of the surface-to-volume ratio on oxidative dehydrogenation of butane in a non-catalytic SiO_2 reactor. The triggering of gas-phase homogeneous reactions by radicals formed by surface reactions during catalytic POX was found for methane by Campbell et al. [36], as well as for POX of butane by Marengo et al. [37]. The latter suggested that fast ignition of exothermic homogeneous reactions by the surface of inert packing material such as SiO_2 was possible in absence of noble metal catalysts during POX of butane, as denoted by the results of the present study. The higher CO selectivity (Fig. 18c) for Al_2O_3/SiO_2 without $Rh/Ce_{0.5}Zr_{0.5}O_2$ was misleading, since the absolute amount of produced CO and H_2 was negligible for both fiber materials below 700℃. This non-noble metal or fiber/sand-catalyzed part of butane conversion competes with the Rh activated part of butane conversion in the actual experiments containing the supported Rh catalyst.

The Rh loading on $Ce_{0.5}Zr_{0.5}O_2$ nanoparticles had an important impact on the reforming performance. However, the amount of catalyst did not affect all reactions taking place in the butane reformer in the same way: While the butane conversion η was remarkably higher for a Rh loading of 2.0 wt% compared to 0.5 wt%, the production of H_2 was almost identical above 600℃ for both loadings (Fig. 19). While the H_2 production for 0.5 wt% Rh exceeded significantly the production of H_2 for 0.25 wt%, the difference in butane conversion and CO production was not large for these Rh loadings. These two effects may again be discussed together with results from reactors containing no Rh-based catalyst at all. Figures 18a and 19a clearly show that the reaction was taking off (light-up) at around 300 ℃ resulting in a butane conversion independent of the Rh loading (Fig. 19a) or the type of fiber plugs (Fig. 18a). The apparent lack of any effect of increasing Rh catalyst loading can now be compared to the lack of CO selectivity and very low H_2 production at 300℃. Apparently, a light-off at 300℃ resulted in preferably full oxidation of butane.

The production of H_2 and CO, indicated by their selectivities, differed in their dependence on reactor temperature. For 2.0 wt% Rh loading and SiO_2 fiber plugs, the H_2 selectivity reached half of its maximum value already below 350℃, whereas the CO selectivity reached this point at around 500℃. The entire temperature dependent behavior showed much higher H_2 selectivity than CO selectivity. This strongly suggests that POX is not the only reaction producing H_2, since POX would have led to similar H_2 and CO selectivities. Instead, the reforming was dominated at lower temperatures by Total Oxidation (TOX) of butane followed by H_2O consuming reactions like Steam Reforming (SR) and Water Gas Shift (WGS). H_2O, which was produced by TOX beside CO_2, reacted with butane by SR to H_2 and CO, where part of this CO reacted subsequently with H_2O by WGS to CO_2 and H_2. This combination of TOX, SR and WGS explained the stronger H_2 production compared to the CO production, which could not be explained by POX alone. For higher temperatures, POX was the dominating reaction, where H_2 and CO were produced likewise. CO_2 producing reactions like TOX and WGS were unimportant for higher temperatures.

This indirect reaction mechanism with POX and TOX followed by SR and reverse WGS was already suggested by Kunimori et al. for butane on platinum [38]. More recently, this autothermal reforming path was investigated by Wang and Gorte for hydrocarbons on Pd/ceria [39]. These studies suggested ceria-supported precious metals as well-suitable catalysts for hydrocarbon reforming catalyzing POX, SR and WGS simultaneously. Wang and Gorte [39] reported a CO selectivity of 6% and butane conversion of 11% at 450℃ using Pd/ceria as catalyst for SR of butane, compared to a maximum CO selectivity of 30% and butane conversion of 71% at the same temperature for the present investigation. At 527℃, Wang and Gorte [40] achieved butane conversion of 41% by SR on Pd/ceria, in contrast to 92% butane conversion at 525℃ for this study. Acharya et al. [41] investigated SR of isobutane on $Pt\text{-}CeO_2\text{-}Gd_2O_3$ and demonstrated butane conversion of 63% and hydrogen yield (as produced hydrogen per hydrogen input from butane and H_2O) of 39% at 600℃, compared to nearly complete butane conversion and 77% hydrogen yield for this investigation at the same temperature. Huff et al. [24] performed POX of butane over Pt coated foam monoliths with $\phi = 0.9$ resulting in butane conversion of 99%, hydrogen yield of 31% and CO selectivity of 79% at 1041℃. For the present study, similar butane conversion and CO selectivity (100% and 77%, respectively) could be obtained at much lower temperature of 675℃ and with a corresponding higher hydrogen yield of 86%. The present investigation on supported Rh catalysts with a very open morphology resulted in higher H_2 and CO yields at lower temperatures compared to other studies, which illustrates the favorable morphological and chemical properties of the aerosol derived ceria/zirconia nanoparticles as a support for Rh. For all measurements, neither significant cracking of butane nor formation of soot could be found, which corresponded well with results from Wang and Gorte [39] and Hilaire et al. [42].

3.4 CONCLUSION

The present work investigated the capability of rhodium doped ceria/zirconia nanoparticles as catalysts for butane-to-syngas reforming at 225 to 750℃. The main issue of this study was to develop a high reforming performance for intermediate temperatures of 500 to 600℃. In this range, a packed bed reactor with catalyst nanoparticles of 2.0 wt% Rh loading and SiO_2-based plugs achieved nearly complete butane conversion with a hydrogen yield ψ of 77%. This resulted in an off-gas containing a H_2 mole fraction X_{H2} of 21% and a CO mole fraction X_{CO} of 13%. In spite of its wide use as a sealing material or monolith base [22-26], the influence of Al_2O_3 in the sealing plugs of the reactor strongly affected the overall performance and suggested a more detailed investigation of non-noble metal catalyzed and homogeneous contributions to butane conversion in such reformer systems. Our results showed that the here-presented reactor configuration may well be suited to provide small and portable butane reforming units for applications together with micro fuel cells.

References

[1] N. Hotz, S.M. Senn and D. Poulikakos, *Exergy analysis of a solid oxide fuel cell micropowerplant*, 158 (2006) 333-347.

[2] G.W. Coffey, J.S. Hardy, L.R. Pederson, P.C. Rieke and E.C. Thomsen, *Oxygen reduction activity of lanthanum strontium nickel ferrite*, 6 (2003) A121-A124.

[3] B. Zhu, *Functional ceria-salt-composite materials for advanced ITSOFC applications*, 114 (2003) 1-9.

[4] B. Zhu, X.T. Yang, J. Xu, Z.G. Zhu, S.J. Ji, M.T. Sun and J.C. Sun, *Innovative low temperature SOFCs and advanced materials*, 118 (2003) 47-53.

[5] R.E. Hayes and S.T. Kolaczkowski, *Mass and Heat-Transfer Effects in Catalytic Monolith Reactors*, 49 (1994) 3587-3599.

[6] O. Deutschmann and L.D. Schmidt, *Modeling the partial oxidation of methane in a short-contact- time reactor*, 44 (1998) 2465-2477.

[7] L.L. Raja, R.J. Kee, O. Deutschmann, J. Warnatz and L.D. Schmidt, *A critical evaluation of Navier-Stokes, boundary-layer, and plug-flow models of the flow and chemistry in a catalytic-combustion monolith*, 59 (2000) 47-60.

[8] A.K. Chaniotis and D. Poulikakos, *Modeling and optimization of catalytic partial oxidation methane reforming for fuel cells*, 142 (2005) 184-193.

[9] L.D. Schmidt, E.J. Klein, C.A. Leclerc, J.J. Krummenacher and K.N. West, *Syngas in millisecond reactors: higher alkanes and fast lightoff*, 58 (2003) 1037-1041.

[10] S.M. Senn and D. Poulikakos, *Tree network channels as fluid distributors constructing double-staircase polymer electrolyte fuel cells*, 96 (2004) 842-852.

[11] M.J. Stutz and D. Poulikakos, *Effects of microreactor wall heat conduction on the reforming process of methane*, 60 (2005) 6983-6997.

[12] R. Schwiedernoch, S. Tischer, C. Correa and O. Deutschmann, *Experimental and numerical study on the transient behavior of partial oxidation of methane in a catalytic, monolith*, 58 (2003) 633-642.

[13] O. Deutschmann, R. Schwiedernoch, L.I. Maier and D. Chatterjee, *Natural Gas Conversion VI*. In: Elsevier, 2001, 251-258.

[14] J.W. Geus and J.C. van Giezen, *Monoliths in catalytic oxidation*, 47 (1999) 169-180.

[15] C.T. Goralski and L.D. Schmidt, *Modeling heterogeneous and homogeneous reactions in the high-temperature catalytic combustion of methane*, 54 (1999) 5791-5807.

[16] S.T. Kolaczkowski, *Modelling catalytic combustion in monolith reactors - challenges faced*, 47 (1999) 209-218.

[17] T. Bruno, A. Beretta, G. Groppi, M. Roderi and P. Forzatti, *A study of methane partial oxidation in annular reactor: activity of Rh/alpha-Al2O3 and Rh/ZrO2 catalysts*, 99 (2005) 89-98.

[18] S. Mazumder and D. Sengupta, *Sub-grid scale modeling of heterogeneous chemical reactions and transport in full-scale catalytic converters*, 131 (2002) 85-97.

[19] E.L. Cussler, *Mass Transfer in Fluid Systems*, Cambridge University Press, 1997.

[20] W.J. Stark, K. Wegner, S.E. Pratsinis and A. Baiker, *Flame aerosol synthesis of vanadia-titania nanoparticles: Structural and catalytic properties in the selective catalytic reduction of NO by NH3*, 197 (2001) 182-191.

[21] A. Trovelli, *Catalysis by ceria and related materials*, Imperial College Press, 2002.

[22] A.S. Bodke, S.S. Bharadwaj and L.D. Schmidt, *The effect of ceramic supports on partial oxidation of hydrocarbons over noble metal coated monoliths*, 179 (1998) 138-149.

[23] D.A. Hickman and L.D. Schmidt, *Production of Syngas by Direct Catalytic-Oxidation of Methane*, 259 (1993) 343-346.

[24] M. Huff, P.M. Torniainen and L.D. Schmidt, *Partial Oxidation of Alkanes over Noble-Metal Coated Monoliths*, 21 (1994) 113-128.

[25] A. Mitri, D. Neumann, T.F. Liu and G. Veser, *Reverse-flow reactor operation and catalyst deactivation during high-temperature catalytic partial oxidation*, 59 (2004) 5527-5534.

[26] B. Silberova, H.J. Venvik, J.C. Walmsley and A. Holmen, *Small-scale hydrogen production from propane*, 100 (2005) 457-462.

[27] L. Madler, H.K. Kammler, R. Mueller and S.E. Pratsinis, *Controlled synthesis of nanostructured particles by flame spray pyrolysis*, 33 (2002) 369-389.

[28] W.J. Stark, L. Madler, M. Maciejewski, S.E. Pratsinis and A. Baiker, *Flame synthesis of nanocrystalline ceria-zirconia: effect of carrier liquid*, (2003) 588-589.

[29] A.B. Bieberle-Hutter, D. Beckel, U.R. Muecke, J.L.M. Rupp, A. Infortuna and L.J. Gauckler, *Micro-Solid Oxide Fuel Cells as Battery Replacement*, 4 (2005) 12-15.
[30] B.C.H. Steele, *Materials for IT-SOFC stacks 35 years R&D: the inevitability of gradualness?*, 134 (2000) 3-20.
[31] R. Burch and E.M. Crabb, *Homogeneous and Heterogeneous Contributions to the Oxidative Dehydrogenation of Propane on Oxide Catalysts*, 100 (1993) 111-130.
[32] K.T. Nguyen and H.H. Kung, *Generation of Gaseous Radicals by a V-Mg-O Catalyst During Oxidative Dehydrogenation of Propane*, 122 (1990) 415-428.
[33] M. Xu and J.H. Lunsford, *Oxidative dehydrogenation of propane*, 57 (1996) 3-11.
[34] M. Huff and L.D. Schmidt, *Production of Olefins by Oxidative Dehydrogenation of Propane and Butane over Monoliths at Short-Contact Times*, 149 (1994) 127-141.
[35] A.A. Lemonidou and A.E. Stambouli, *Catalytic and non-catalytic oxidative dehydrogenation of n-butane*, 171 (1998) 325-332.
[36] K.D. Campbell, E. Morales and J.H. Lunsford, *Gas-Phase Coupling of Methyl Radicals During the Catalytic Partial Oxidation of Methane*, 109 (1987) 7900-7901.
[37] S. Marengo, P. Comotti and G. Galli, *New insight into the role of gas phase reactions in the partial oxidation of butane*, 81 (2003) 205-213.
[38] K. Kunimori, T. Iwade, H. Uetsuka, S. Ito and T. Watanabe, *Infrared Chemiluminescence Study of Co Produced by Partial Oxidation of Butane on Platinum*, 18 (1993) 253-259.
[39] X. Wang and R.J. Gorte, *A study of steam reforming of hydrocarbon fuels on Pd/ceria*, 224 (2002) 209-218.
[40] X. Wang and R.J. Gorte, *Steam reforming of n-butane on Pd/ceria*, 73 (2001) 15-19.
[41] C.K. Acharya, A.M. Lane and T.R. Krause, *Kinetic study of the steam reforming of isobutane using a Pt-CeO2-Gd2O3 Catalyst*, 106 (2006) 41-48.
[42] S. Hilaire, S. Sharma, R.J. Gorte, J.M. Vohs and H.W. Jen, *Effect of SO2 on the oxygen storage capacity of ceria-based catalysts*, 70 (2000) 131-135.